# A Novel Tensor-Based Hyperspectral Image Restoration Method With Low-Rank Modeling in Gradient Domains

Pengfei Liu, Lanlan Liu, and Liang Xiao, *Member, IEEE*

***Abstract*—The hyperspectral image (HSI) is easily contaminated by various kinds of mixed noise (such as Gaussian noise, impulse noise, stripes, and deadlines) during the process of data acquisition and conversion, which significantly affect the quality and applications of HSI. As an important and effective scheme for the quality improvement of HSI, the HSI restoration problem aims to recover a clean HSI from the noisy HSI with mixed noise. Thus, based on the tensor modeling of HSI, we propose a novel tensor-based HSI restoration model with low-rank modeling in gradient domains in a unified tensor representation framework in this article. First, for the spectral low-rank modeling of HSI in spectral gradient domain, we particularly exploit the low-rank property of spectral gradient, and propose the spectral gradient-based weighted nuclear norm low-rank prior term. Second, for the spatial-mode low-rank modeling of HSI in spatial gradient domain, we particularly exploit the low-rank property of spatial gradient tensors via the discrete Fourier transform, and propose the spatial gradient-based tensor nuclear norm low-rank prior term. Then, we use the alternative direction method of multipliers to solve the proposed model. Finally, the restoration results on both the simulated and real HSI datasets demonstrate that the proposed method is superior to many state-of-the-art methods in the aspects of visual and quantitative comparisons.**

***Index Terms*—Hyperspectral image restoration, low-rank priors, spectral and spatial gradient domain, tensor nuclear norm (TNN).**

## I. Introduction

HYPERSPECTRAL images (HSIs) contain hundreds of bands and rich spectral information, so they are widely used in various fields of feature extraction, classification, unmixing, target detection, super resolution, and fusion [1], [2], [3], [4], [5], [6]. However, due to the influence of acquisition equipment and external environment, HSIs are usually contaminated by various kinds of mixed noise (such as, Gaussian noise, impulse noise, deadlines, and stripes), which not only affects the image quality, but also limits the later processing and applications of HSI. Therefore, HSI restoration, which is recently an important scheme to remove the mixed noise so as to improve the image quality of HSI, has very important research and application significance. Specifically, as an effective way to remove the noise, the core of image priors-based HSI restoration model is to make full use of the effective spectral and spatial priors of HSI, such as, nonlocal self-similarity, spatial-spectral smoothness, and low-rank priors [7], [8], [9].

As we know, the nonlocal self-similarity was earlier used for grayscale image denoising, which assumed that a grayscale image contained lots of similar 2-D blocks (i.e., patches) at different positions of the image. Then, many traditional methods using spatial nonlocal self-similarity were generalized to denoise HSI band by band, such as block matching and 3-D filtering (BM3D) [10], dictionary learning [11], and nonlocal means filter [12], [13]. However, these methods treated each band of HSI as a grayscale image, which did not consider the important correlation between spectral bands, so the restoration performance was not very ideal and could be further improved. To solve this problem, scholars investigated the spatial and spectral nonlocal self-similarity-based restoration methods using similar 3-D cubes to replace the common 2-D blocks, such as MSPCA-BM3D [14], BM4D [15], 3-D nonlocal sparse (3DNLS) [16], and nonlocal tensor dictionary learning [17].

More clearly, the methods based on low-rank priors have been extensively studied and achieved great success in the field of HSI restoration. Specifically, inspired by the robust principal component analysis (RPCA) model [18], which modeled the observed data as the sum of a low-rank matrix and a sparse matrix, Zhang et al. [19] proposed the low-rank matrix restoration (LRMR) model. Moreover, Chen et al. [20] proposed a nonconvex low-rank matrix approximation (NonLRMA) model, which used a nonconvex regularizer to replace the traditional nuclear norm, so the rank function can be better approximated. Although LRMR can effectively remove the mixed noise in HSI, it does not impose any spatial constraints on the neighboring pixels of HSI. To solve this problem, Zhu et al. [21] considered both spectral and spatial constraints to preserve the fine structure of

Manuscript received 5 October 2022; revised 19 November 2022; accepted 10 December 2022. Date of publication 13 December 2022; date of current version 21 December 2022. This work was supported in part by the China Postdoctoral Science Foundation under Grant 2022M711692, in part by the National Natural Science Foundation of China under Grant 61802202, and in part by the Fundamental Research Funds for the Central Universities under Grant JSGP202204. *(Corresponding author: Pengfei Liu.)*

Pengfei Liu and Lanlan Liu are with the School of Computer Science, Nanjing University of Posts and Telecommunications, Nanjing 210023, China, and also with the Jiangsu Key Laboratory of Big Data Security and Intelligent Processing, Nanjing 210023, China (e-mail: liupengfei199091@163.com; 1020041114@njupt.edu.cn).

Liang Xiao is with the School of Computer Science and Engineering, Nanjing University of Science and Technology, Nanjing 210094, China, and also with the Jiangsu Key Laboratory of Spectral Imaging and Intelligent Sense, Nanjing 210094, China (e-mail: xiaoliang@mail.njust.edu.cn).

Digital Object Identifier 10.1109/JSTARS.2022.3228942

HSI, and proposed the spectral nonlocal low-rank model. Based on the LRMR model, He et al. [22] proposed the noise-adjusted iterative low-rank matrix approximation (NAILRMA) method, which considered the different noise in different bands and can well remove the noise from HSI. However, when the local noise is larger, the denoising performance will become worse. To address this shortcoming, Wang et al. [23] proposed the group low-rank representation model, where the local similarity within patches and the nonlocal similarity between groups of patches were both used to preserve the HSI image features and remove the noise. What is more, Fan et al. [24] proposed the superpixel segmentation and low-rank representation (SSLRR) model to remove different types of noise.

Moreover, since the total variation (TV) regularization method [25] can effectively preserve shape edges and enhance piecewise smoothness, then various TV-based spatial-spectral smoothness prior models are also proposed for HSI restoration, such as cubic TV (CTV) [26], spectral-spatial adaptive hyperspectral TV (SSAHTV) [27], spectrally adaptive multidimensional nonlocal total variation (SAMNLTV) [28], and spatio-spectral TV (SSTV) [29]. Although these methods fully use the local spatial and spectral information of HSI, they ignore the low-rank characteristics of HSI. Based on this, He et al. [30] proposed the TV-regularized low-rank matrix factorization (LRTV) model, which introduced the band-by-band TV regularization term and the low-rank prior together for HSI restoration. However, LRTV considered the TV model separately for each spectral band, ignoring the spectral smoothness of HSI. To overcome this drawback, Wang et al. [31] used the SSTV [29] to model the spatial-spectral smoothness of HSI, and proposed the low-rank constraint and spatial spectral total variation (LSSTV) model, which can effectively remove the mixed noise and preserve the edge structure. Moreover, He et al. [32] further used the anisotropic spatial-spectral TV to model the global spatial and spectral smoothness and consistency of HSI, and proposed the local low-rank matrix recovery and global spatial-spectral TV (LLRSSTV) model, which can effectively separate the sparse noise.

However, these above low rank-based methods usually need to rearrange the HSI cube into the matrix for low-rank modeling, it is easy to destroy the correlation between spectral bands. To overcome these drawbacks, treating HSI as a third-order tensor had been recently and widely studied to maintain the cube structure of HSI. Thus, many tensor low-rank-based HSI restoration methods had been proposed, such as the low-rank tensor approximation (LRTA) model [33], TV regularized low-rank tensor decomposition (LRTDTV) [34], double-factor-regularized low-rank tensor factorization (LRTFDFR) [35], low-rank tensor dictionary learning denoising method [36], weighted tensor low-rank restoration (WLRTR) model [37], global spatial-spectral TV regularized nonconvex local low-rank tensor approximation (LLxRGTV) [38], etc.

Among the tensor decomposition-based HSI denoising methods, the Tucker decomposition [39] and CANDECOMP/PARAFAC (CP) decomposition [40] schemes are commonly used to model the low-rank property of tensors, such as rank-1 tensor decomposition (R1TD) [41], nonlocal low-rank regularized R1TD (NLR-R1TD) [42], nonlocal similarity-based nonnegative Tucker decomposition [43], PARAFAC model [44], and nonlocal low-rank regularized tensor CP decomposition [45]. However, these two decompositions cannot give the best approximation to the tensor, Chen et al. [46] further proposed the nonlocal tensor-ring (TR) approximation, and exploited the nonlocal self-similarity and global spectral correlation of HSI at the same time to improve the restoration performance. More specifically, different from CP decomposition and Tucker decomposition, Kilmer et al. [47] defined tube rank and multirank of tensor based on tensor singular value decomposition (t-SVD), which can better describe the low-rank property of tensor. On this basis, by applying the discrete Fourier transform (DFT) along the mode-3 of the tensor, Zhang et al. [48] then defined the tensor nuclear norm (TNN) as the sum of singular values of all the frontal slices as the convex approximation of tensor rank function. However, TNN only describes the low rankness of spectral mode, but ignores the spatial modes. To model the low rankness of the spectral and spatial modes of HSI at the same time, Zheng et al. [49] extended t-SVD to mode-k t-SVD, then exploited the tensor low-rank property of HSI via the DFT along spectral and spatial modes, and particularly proposed the tensor fiber rank model and its convex relaxation model, namely, the 3-D tensor nuclear norm (3DTNN) model. Furthermore, some HSI restoration methods based on low-rank modeling in the transformed domain are also proposed, such as the framelet-based three-modal tensor nuclear norm (F-3MTNN) model [50] and the factor group sparsity-regularized nonconvex low-rank approximation (FGSLR) model [51]. What is more, some new low-rank tensor representation models are recently proposed for HSI restoration especially for HSI completion and cloud removal, such as the multilayer sparsity-based tensor decomposition (MLSTD) model [52], the parametric tensor sparsity model based on Laplacian scale mixture modeling via three-layer transform (LSM-TLT) [53], and the multimodal core tensor factorization (MCTF) model [54].

More recently, the deep learning-based HSI restoration approaches have attracted more attention and became more popular, such as the convolutional neural network (CNN)-based HSI denoising method (HSI-DeNet) [55], which modeled HSIs as tensors and well treated various noise simultaneously, and the HSI denoising with spatial-spectral deep residual CNN method (HSID-CNN) [56], which used spatial-spectral multiscale feature extraction and deep CNN-based residual learning to obtain a nonlinear mapping between the clean and noisy HSIs.

More clearly, the tensor construction and its tensor low-rank property modeling of HSI are the core of the tensor low-rank prior-based HSI restoration methods. Thus, we also focus on the tensor low-rank-based prior methods for HSI restoration, and particularly aim to investigate more effective scheme for the tensor construction and tensor low-rank modeling of spectral and spatial modes in this article.

To the best of our knowledge, there are some methods based on the gradient-based low-rank modeling for image processing. For example, the enhanced 3DTV (E-3DTV) model [57] has exploited the low-rankness of unfolded spatial gradients, i.e., the matrix-based low-rank property, not in the tensor form, and

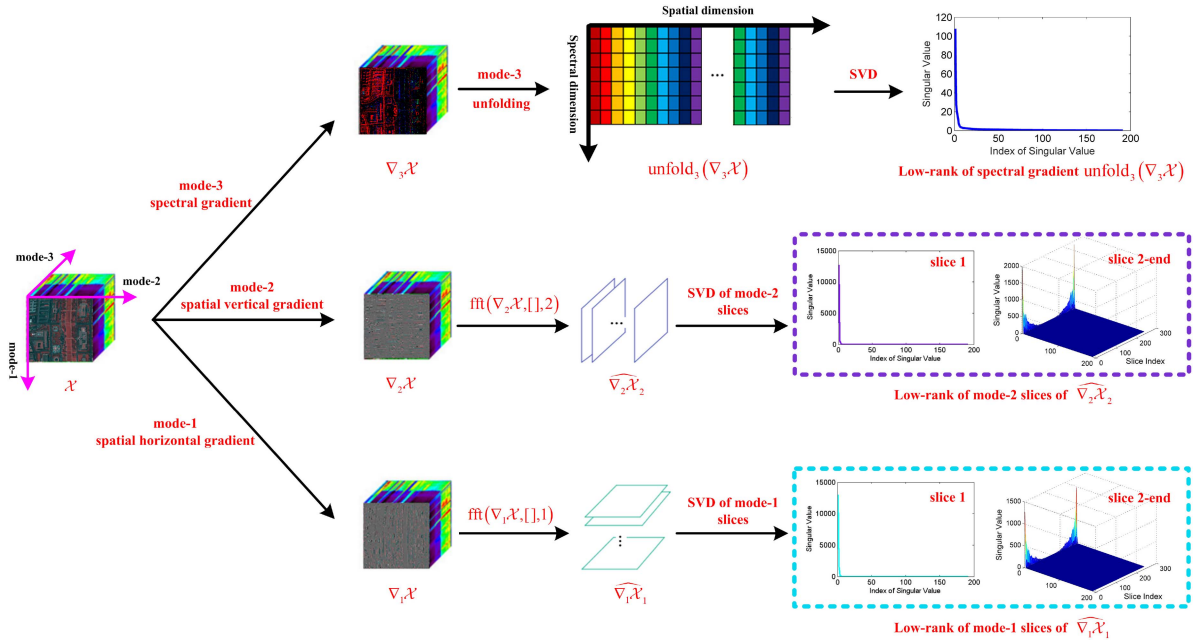


Fig. 1. Flowchart of low-rank modeling in gradient domains.

the gradient-based low-rank approximation (Grad-LR) model [58] just exploits the nonlocal 2-D patched-based low rankness of the spatial gradients for 2-D image inpainting, not in the tensor form either. More clearly, there are no relative works to investigate the spatial gradient tensors based low-rank properties in the tensor form for the HSI restoration recently. Thus, the low-rank modeling of HSI in the spatial gradient domain in the tensor form is highly valuable to be exploited for spatial-spectral structure preservation.

Moreover, by comparing with the strong tensor fiber low-rank property of spatial mode, the tensor fiber low-rank property of spectral mode are relatively unsuitable for spectral low-rank modeling of HSI in the 3DTNN method [49], owing to the HSI clearly shows strong spectral low-rank property of spectral mode in the original domain [19], [30]. Thus, the spectral low-rank property of spectral mode of HSI needs to be suitably modeled.

Based on the above analysis, instead of directly treating the HSI as a third-order tensor for tensor low-rank modeling in the original domain, we thus construct the spatial gradient tensors and the spectral gradient tensor for HSI, and particularly investigate the low-rank properties of HSI in gradient domains in this article. Specifically, the main contributions of this article are described as follows:

1) For the HSI, we first obtain its spatial horizontal gradient tensor and spatial vertical gradient tensor in spatial gradient domain, and the spectral gradient tensor in spectral gradient domain. Then, for the spectral low-rank prior modeling of HSI in spectral gradient domain, we particularly investigate the low-rank property of the spectral gradient of HSI to establish the spectral gradient-based weighted nuclear norm low-rank prior term (see Fig. 1), which can effectively remove the structural noise, such as stripes and deadlines.

2) For the spatial low-rank prior modeling of HSI in spatial gradient domain, we consider to use the DFT along the spatial mode-1 of spatial horizontal gradient tensor and the spatial mode-2 of spatial vertical gradient tensor of HSI, and obtain the spatial mode-1 gradient frequency tensor and the spatial mode-2 gradient frequency tensor, respectively. Furthermore, the low-rank property of the spatial mode-1 gradient frequency tensor and the spatial mode-2 gradient frequency tensor is modeled by the unified spatial gradient-based TNN low-rank prior term (see Fig. 1).

3) Consequently, based on the spectral gradient-based weighted nuclear norm low-rank prior term and the spatial gradient-based TNN low-rank prior, we propose a novel unified tensor-based HSI restoration model with low-rank modeling in gradient domains in this article.

The rest part of the article are listed as follows. We proposed the unified tensor-based HSI restoration model with low-rank modeling in gradient domains in Section II, and solved the proposed model in Section III. Section IV showed the overall experimental results and analysis. Section V provided the discussion in detail. Finally, the conclusion was given in Section VI.

## II. Proposed Model

In this section, a unified tensor-based HSI restoration model with low-rank modeling in gradient domains will be proposed. For better modeling and analyzing, we first give some important symbols in Table I.

### A. Formulation of HSI Restoration Problem

In fact, HSI is a cube data, which can be modeled as a third-order tensor. More clearly, let $\mathcal{X} \in \Re^{n_1 \times n_2 \times n_3}$ to be the original clean HSI, and $\mathcal{Y} \in \Re^{n_1 \times n_2 \times n_3}$ to be the noisy HSI with Gaussian noise and sparse noise (such as impulse noise, stripes, and deadlines), where $n_1 \times n_2$ is the size of spatial dimension,

TABLE I
DEFINITIONS OF SYMBOLS

| Symbols | Definitions |
|---|---|
| $x$, $\mathbf{x}$, $\mathbf{X}$ | scalar, vector, matrix |
| $\mathcal{X} \in \Re^{n_1 \times n_2 \times n_3}$ | third-order tensor |
| $\mathcal{X}_{i_1,i_2,i_3}$ | $(i_1,i_2,i_3)$-th element of $\mathcal{X}$ |
| $\mathcal{X}(i_1,:,:), \mathcal{X}(:,i_2,:), \mathcal{X}(:,:,i_3)$ | $i$-th mode-$k$ slice of $\mathcal{X}$ |
| $\text{unfold}_k(\mathcal{X})$ | mode-$k$ unfolding of $\mathcal{X}$ |
| $\|\mathcal{X}\|_F = \sqrt{\sum_{i_1,i_2,i_3} \|\mathcal{X}_{i_1,i_2,i_3}\|^2}$ | Frobenius norm of $\mathcal{X}$ |
| $\|\mathcal{X}\|_1 = \sum_{i_1,i_2,i_3} \|\mathcal{X}_{i_1,i_2,i_3}\|$ | $l_1$ norm of $\mathcal{X}$ |
| $\widehat{\mathcal{X}}_k = \text{fft}(\mathcal{X},[],k)$ | discrete Fourier transform of $\mathcal{X}$ along mode-$k$ |
| $\sigma_j(\mathbf{X})$ | $j$-th singular value of $\mathbf{X}$ |
| $\|\mathbf{X}\|_* = \sum_j \sigma_j(\mathbf{X})$ | nuclear norm of $\mathbf{X}$ |
| $\|\mathbf{X}\|_{\mathbf{w},*} = \sum_j w_j \sigma_j(\mathbf{X})$ | weighted nuclear norm of $\mathbf{X}$ |

and $n_3$ is the number of spectral bands. Therefore, the HSI with Gaussian noise and sparse noise contaminated can be expressed as

$$\mathcal{Y} = \mathcal{X} + \mathcal{N} + \mathcal{S} \tag{1}$$

where $\mathcal{N} \in \Re^{n_1 \times n_2 \times n_3}$ and $\mathcal{S} \in \Re^{n_1 \times n_2 \times n_3}$ are the Gaussian noise and sparse noise, respectively.

The goal of HSI restoration is to restore the clean HSI $\mathcal{X}$ from the noisy HSI $\mathcal{Y}$. By imposing the effective prior knowledge of the clean HSI $\mathcal{X}$ and the sparse noise $\mathcal{S}$, thus, the image prior-based HSI restoration model can be expressed as

$$\min_{\mathcal{X},\mathcal{S}} \frac{1}{2} \|\mathcal{Y} - \mathcal{X} - \mathcal{S}\|_F^2 + \lambda_1 R(\mathcal{S}) + \beta J(\mathcal{X}) \tag{2}$$

where $\frac{1}{2}\|\mathcal{Y} - \mathcal{X} - \mathcal{S}\|_F^2$ is the fidelity term modeling the Gaussian noise $\mathcal{N}$, $R(\mathcal{S}) = \|\mathcal{S}\|_1$ is the sparse prior regularization term modeling the sparse noise $\mathcal{S}$, $J(\mathcal{X})$ is the prior regularization term modeling the spatial and spectral properties of the clean HSI $\mathcal{X}$, $\lambda_1$ and $\beta$ are the tradeoff parameters used to balance the two prior regularization terms.

### B. Low-Rank Modeling in Spectral Gradient Domain

*1) Motivation:* Clearly, we know that the common idea for spectral low-rank modeling used in the previous methods is that the spectra of HSI $\mathcal{X} \in \Re^{n_1 \times n_2 \times n_3}$ is low rank, namely, the matrix $\text{unfold}_3(\mathcal{X}) \in \Re^{n_3 \times n_1 n_2}$ is low rank [19], [30], and then the nuclear norm-based spectral low-rank prior is usually enforced as

$$J_1(\mathcal{X}) = \|\text{unfold}_3(\mathcal{X})\|_*. \tag{3}$$

Moreover, we also considered that the previous spatial-spectral smoothness-based methods usually used the spectral gradient-based term $\|\nabla_3 \mathcal{X}\|_1$ to enforce the *sparsity* of spectral gradient for spectral information preserving, where $\nabla_3$ is the spectral gradient operator. Thus, we mainly investigate the low-rank prior modeling of HSI in spectral gradient domain in this article.

Inspired by them, we mainly aim to model the spectral smoothness and spectral low-rankness of HSI in the spectral gradient domain at the same time in this article. To this end, we particularly investigate the low-rank prior modeling of the spectral gradient of HSI and establish the spectral gradient-based weighted nuclear norm low-rank prior model.

*2) Spectral Gradient-Based Weighted Nuclear Norm Low-Rank Prior Term:* Specifically, $\nabla_3$ represents the spectral gradient operator along the mode-3 spectral dimension of HSI $\mathcal{X}$, then the spectral gradient of HSI $\mathcal{X}$ is expressed as

$$\nabla_3 \mathcal{X}(i_1,i_2,i_3) = \mathcal{X}(i_1,i_2,i_3+1) - \mathcal{X}(i_1,i_2,i_3). \tag{4}$$

As clearly shown in Fig. 1, for HSI $\mathcal{X} \in \Re^{n_1 \times n_2 \times n_3}$, we can obtain its spectral gradient tensor $\nabla_3 \mathcal{X} \in \Re^{n_1 \times n_2 \times n_3}$. Then, by arranging $\nabla_3 \mathcal{X}$ into a matrix $\text{unfold}_3(\nabla_3 \mathcal{X}) \in \Re^{n_3 \times n_1 n_2}$ via the mode-3 unfolding operation, and performing singular value decomposition (SVD) on $\text{unfold}_3(\nabla_3 \mathcal{X})$, we can clearly obtain the low-rank property of $\text{unfold}_3(\nabla_3 \mathcal{X})$ in Fig. 1. Therefore, the low-rank property of $\text{unfold}_3(\nabla_3 \mathcal{X})$ is particularly modeled by the following spectral gradient-based weighted nuclear norm low-rank prior term, which is formulated as

$$J_2(\mathcal{X}) = \lambda_2 \|\text{unfold}_3(\nabla_3 \mathcal{X})\|_{\mathbf{w},*} \tag{5}$$

where $t = \min\{n_3, n_1 n_2\}$, $\mathbf{w} = (w_1, \ldots, w_t)^T \in \Re^t$ is the vector of the weights with $w_j = 1/(\sigma_j(\text{unfold}_3(\nabla_3 \mathcal{X})) + \varepsilon)$, $j = 1, \ldots, t$, $\varepsilon$ is a very small positive scalar, and $\lambda_2 \geq 0$.

### C. Low-Rank Modeling in Spatial Gradient Domain

*1) Motivation:* First, we considered that the 3DTNN method [49] exploited the tensor low-rank property of HSI in original domain by applying the DFT along each mode of HSI $\mathcal{X}$ to form the DFT-based HSIs $\widehat{\mathcal{X}}_1 = \text{fft}(\mathcal{X},[],1)$, $\widehat{\mathcal{X}}_2 = \text{fft}(\mathcal{X},[],2)$, and $\widehat{\mathcal{X}}_3 = \text{fft}(\mathcal{X},[],3)$, and obtained that the slices of each mode of the DFT-based HSIs are low rank. Clearly, the 3DTNN prior term was proposed as

$$\|\mathcal{X}\|_{\text{3DTNN}} = \sum_{k=1}^{3} \xi_k \|\mathcal{X}\|_{\text{TNN}_k} \tag{6}$$

where $\xi_k \geq 0$ such that $\sum_{k=1}^{3} \xi_k = 1$, and $\|\mathcal{X}\|_{\text{TNN}_k}$ is the DFT-based mode-$k$ TNN of $\mathcal{X}$, which is defined as

$$\begin{cases} \|\mathcal{X}\|_{\text{TNN}_1} = \sum_{i=1}^{n_1} \left\| \widehat{\mathcal{X}}_1(i,:,:) \right\|_* \\ \|\mathcal{X}\|_{\text{TNN}_2} = \sum_{i=1}^{n_2} \left\| \widehat{\mathcal{X}}_2(:,i,:) \right\|_* \\ \|\mathcal{X}\|_{\text{TNN}_3} = \sum_{i=1}^{n_3} \left\| \widehat{\mathcal{X}}_3(:,:,i) \right\|_*. \end{cases} \tag{7}$$

Moreover, we also considered that the previous spatial-spectral smoothness-based methods usually used the spatial gradients-based prior term $\sum_i^2 \rho_i \|\nabla_i \mathcal{X}\|_1$ to enforce the *sparsity* of spatial gradients, where $\nabla_1$ and $\nabla_2$ are the spatial horizontal and vertical gradient operators. Specifically, as Section I mentioned, the enhanced 3DTV (E-3DTV) model [57] has exploited the low rankness of unfolded spatial gradients, i.e., the matrix-based low-rank property, not in the tensor form, and the gradient-based low-rank approximation (Grad-LR) model [58]

just exploits the nonlocal 2-D patched-based low rankness of the spatial gradients for 2-D image inpainting, not in the tensor form either. More clearly, there are no relative works to investigate the spatial gradient tensors-based low-rank properties in the tensor form for HSI restoration recently. Thus, the low-rank modeling of HSI in the spatial gradient domain in the tensor form is highly valuable to be exploited for spatial-spectral structure preservation.

Thus, for the spatial-mode low-rank modeling, instead of directly treating the HSI as a third-order tensor for tensor low-rank modeling of 3DTNN method [49] in the original domain, we mainly investigate the spatial gradient tensors and tensor low-rank priors of HSI in the spatial gradient domain in this article. Specifically, inspired by the 3DTNN method, we still apply the DFT but to the spatial gradients of HSI, and obtain that the spatial gradient tensors in the DFT domain are also low rank, and particularly propose the following spatial gradient-based TNN low-rank prior term.

*2) Spatial Gradient-Based TNN Low-Rank Prior Term:* Thus, for the tensor construction, we first apply the spatial horizontal gradient operator $\nabla_1$ and the spatial vertical gradient operator $\nabla_2$ to the HSI $\mathcal{X} \in \Re^{n_1 \times n_2 \times n_3}$, and obtain its spatial horizontal gradient tensor $\nabla_1 \mathcal{X} \in \Re^{n_1 \times n_2 \times n_3}$ and spatial vertical gradient tensor $\nabla_2 \mathcal{X} \in \Re^{n_1 \times n_2 \times n_3}$, which are defined as

$$\begin{cases} \nabla_1 \mathcal{X}\left(i_1, i_2, i_3\right) = \mathcal{X}\left(i_1+1, i_2, i_3\right) - \mathcal{X}\left(i_1, i_2, i_3\right) \\ \nabla_2 \mathcal{X}\left(i_1, i_2, i_3\right) = \mathcal{X}\left(i_1, i_2+1, i_3\right) - \mathcal{X}\left(i_1, i_2, i_3\right). \end{cases} \tag{8}$$

Then, we use the DFT along the spatial mode-1 of spatial horizontal gradient tensor $\nabla_1 \mathcal{X}$ and the spatial mode-2 of spatial vertical gradient tensor $\nabla_2 \mathcal{X}$, respectively. Thus, we obtain the spatial mode-1 horizontal gradient frequency tensor $\widehat{\nabla_1 \mathcal{X}}_1 = \text{fft}(\nabla_1 \mathcal{X}, [\,], 1) \in \Re^{n_1 \times n_2 \times n_3}$ and the spatial mode-2 vertical gradient frequency tensor $\widehat{\nabla_2 \mathcal{X}}_2 = \text{fft}(\nabla_2 \mathcal{X}, [\,], 2) \in \Re^{n_1 \times n_2 \times n_3}$, respectively. Finally, we particularly exploit the tensor low-rank property of $\widehat{\nabla_1 \mathcal{X}}_1$ and $\widehat{\nabla_2 \mathcal{X}}_2$ in Fig. 1.

As clearly shown in Fig. 1, the slices of $\widehat{\nabla_1 \mathcal{X}}_1$ along mode-1 and the slices of $\widehat{\nabla_2 \mathcal{X}}_2$ along mode-2 are low rank, respectively. Thus, the low rankness of the spatial mode-1 horizontal gradient frequency tensor $\widehat{\nabla_1 \mathcal{X}}_1$ and the spatial mode-2 vertical gradient frequency tensor $\widehat{\nabla_2 \mathcal{X}}_2$ is modeled by the mode-1 and mode-2 TNNs, respectively. Furthermore, we propose the unified spatial gradient-based TNN low-rank (SGTNNLR) prior term, which is formulated as

$$\begin{aligned} J_3(\mathcal{X}) &= \alpha_1 \|\nabla_1 \mathcal{X}\|_{\text{TNN}_1} + \alpha_2 \|\nabla_2 \mathcal{X}\|_{\text{TNN}_2} \\ &= \sum_{k=1}^{2} \alpha_k \|\nabla_k \mathcal{X}\|_{\text{TNN}_k} \end{aligned} \tag{9}$$

where $\alpha_1 \geq 0$, $\alpha_2 \geq 0$, and $\|\nabla_k \mathcal{X}\|_{\text{TNN}_k}$ is the DFT-based mode-$k$ TNN of $\nabla_k \mathcal{X}$, which is defined as

$$\begin{cases} \|\nabla_1 \mathcal{X}\|_{\text{TNN}_1} = \sum_{i=1}^{n_1} \left\| \widehat{\nabla_1 \mathcal{X}}_1\left(i, :, :\right) \right\|_* \\ \|\nabla_2 \mathcal{X}\|_{\text{TNN}_2} = \sum_{i=1}^{n_2} \left\| \widehat{\nabla_2 \mathcal{X}}_2\left(:, i, :\right) \right\|_* \end{cases} \tag{10}$$

where $\widehat{\nabla_1 \mathcal{X}}_1(i, :, :)$ and $\widehat{\nabla_2 \mathcal{X}}_2(:, i, :)$ are the $i$th mode-1 slice of $\widehat{\nabla_1 \mathcal{X}}_1$ and $i$th mode-2 slice of $\widehat{\nabla_2 \mathcal{X}}_2$, respectively.

### D. Proposed Model

Based on above model (2), we combine the spectral gradient-based weighted nuclear norm low-rank prior term (5) and the spatial gradient-based TNN low-rank prior term (9), and propose the unified tensor-based HSI restoration model with low-rank modeling in gradient domains as

$$\begin{aligned} \min_{\mathcal{X}, \mathcal{S}} \ & \tfrac{1}{2} \|\mathcal{Y} - \mathcal{X} - \mathcal{S}\|_F^2 + \lambda_1 \|\mathcal{S}\|_1 \\ & + \lambda_2 \|\text{unfold}_3(\nabla_3 \mathcal{X})\|_{\mathbf{w},*} + \sum_{k=1}^{2} \alpha_k \|\nabla_k \mathcal{X}\|_{\text{TNN}_k}. \end{aligned} \tag{11}$$

## III. Algorithm

Clearly, we here apply the ADMM method to solve the proposed model (11). By setting three auxiliary variables $\mathcal{L}$, $\mathcal{W}_1$, and $\mathcal{W}_2$, the model (11) is equivalently transformed into the following form:

$$\begin{aligned} \min_{\mathcal{X}, \mathcal{S}, \mathcal{W}_k, \mathcal{L}} \ & \tfrac{1}{2} \|\mathcal{Y} - \mathcal{X} - \mathcal{S}\|_F^2 + \lambda_1 \|\mathcal{S}\|_1 \\ & + \lambda_2 \|\text{unfold}_3(\mathcal{L})\|_{\mathbf{w},*} + \sum_{k=1}^{2} \alpha_k \|\mathcal{W}_k\|_{\text{TNN}_k} \\ \text{s.t.} \quad & \mathcal{L} = \nabla_3 \mathcal{X}, \quad \mathcal{W}_1 = \nabla_1 \mathcal{X}, \quad \mathcal{W}_2 = \nabla_2 \mathcal{X}. \end{aligned} \tag{12}$$

Then, its augmented Lagrange function is expressed as

$$\begin{aligned} \min_{\mathcal{X}, \mathcal{S}, \mathcal{W}_k, \mathcal{L}} \ & \tfrac{1}{2} \|\mathcal{Y} - \mathcal{X} - \mathcal{S}\|_F^2 + \lambda_1 \|\mathcal{S}\|_1 \\ & + \lambda_2 \|\text{unfold}_3(\mathcal{L})\|_{\mathbf{w},*} + \sum_{k=1}^{2} \alpha_k \|\mathcal{W}_k\|_{\text{TNN}_k} \\ & + \tfrac{\eta}{2} \|\mathcal{L} - \nabla_3 \mathcal{X} - \mathcal{U}\|_F^2 + \sum_{k=1}^{2} \tfrac{\mu_k}{2} \|\mathcal{W}_k - \nabla_k \mathcal{X} - \mathcal{H}_k\|_F^2 \end{aligned} \tag{13}$$

where $\eta$, $\mu_1$, and $\mu_2$ are the penalty parameters and $\mathcal{U}$, $\mathcal{H}_1$, and $\mathcal{H}_2$ are the Lagrange multipliers.

Thus, by initializing $\mathcal{X}^{(0)}$, $\mathcal{S}^{(0)}$, $\mathcal{L}^{(0)}$, $\mathcal{U}^{(0)}$, $\mathcal{W}_k^{(0)}$, $\mathcal{H}_k^{(0)}$, $(k = 1, 2)$ and using the iterative procedure, the optimization of (13) is decomposed into the optimization of the following four subproblems under the ADMM framework.

*1) Optimization of $\mathcal{S}$:* The subproblem of $\mathcal{S}^{(i+1)}$ is given as

$$\min_{\mathcal{S}} \frac{1}{2} \left\| \mathcal{Y} - \mathcal{X}^{(i)} - \mathcal{S} \right\|_F^2 + \lambda_1 \|\mathcal{S}\|_1 \tag{14}$$

which can be efficiently solved by the soft-thresholding method as

$$\mathcal{S}^{(i+1)} = \text{shrink}\left( \mathcal{Y} - \mathcal{X}^{(i)}, \lambda_1 \right) \tag{15}$$

where $\text{shrink}(Q, \delta) = \text{sign}(Q) \max(0, |Q| - \delta)$ is the soft-thresholding operator with threshold value $\delta$.

*2) Optimization of $\mathcal{L}$:* The subproblem of $\mathcal{L}^{(i+1)}$ is given as

$$\min_{\mathcal{L}} \frac{\eta}{2} \left\| \mathcal{L} - \nabla_3 \mathcal{X}^{(i)} - \mathcal{U}^{(i)} \right\|_F^2 + \lambda_2 \|\text{unfold}_3(\mathcal{L})\|_{\mathbf{w}^{(i)},*} \tag{16}$$

where the weight vector $\mathbf{w}^{(i)} = (w_1^{(i)}, \ldots, w_t^{(i)})^T \in \Re^t$ consists of each element $w_j^{(i)} = 1/(\sigma_j(\text{unfold}_3(\nabla_z \mathcal{X}^{(i)})) + \varepsilon)$, $j = 1, \ldots, t$ and $t = \min\{n_3, n_1 n_2\}$.

By using the mode-3 unfolding operation, $\mathcal{L}^{(i+1)}$ subproblem is equivalent to the following form of $\mathrm{unfold}_3(\mathcal{L}^{(i+1)})$ subproblem:

$$\min_{\mathrm{unfold}_3(\mathcal{L})} \frac{\eta}{2}\left\|\mathrm{unfold}_3(\mathcal{L})-\mathrm{unfold}_3(\nabla_3\mathcal{X}^{(i)}+\mathcal{U}^{(i)})\right\|_F^2 +\lambda_2\|\mathrm{unfold}_3(\mathcal{L})\|_{\mathbf{w}^{(i)},*}. \tag{17}$$

Thus, the weighted singular value soft-thresholding method [59] is used to solve the $\mathrm{unfold}_3(\mathcal{L}^{(i+1)})$ subproblem (17) as

$$\mathrm{unfold}_3(\mathcal{L}^{(i+1)})=\mathcal{D}_{\mathbf{w}^{(i)},\lambda_2/\eta}\left(\mathrm{unfold}_3(\nabla_3\mathcal{X}^{(i)}+\mathcal{U}^{(i)})\right) \tag{18}$$

where $\mathcal{D}_{\mathbf{w}^{(i)},\tau}(\cdot)$ is the generalized soft-thresholding operator with weight vector $\mathbf{w}^{(i)}$ and defined as

$$\begin{aligned}\mathcal{D}_{\mathbf{w}^{(i)},\tau}(\mathbf{E}) &= \mathbf{A}\,\mathcal{D}_{\mathbf{w}^{(i)},\tau}(\mathbf{\Sigma})\,\mathbf{B}\\ &= \mathbf{A}\ \mathrm{diag}\left\{\max\left(0,\ \delta_j-\tau w_j^{(i)}\right)\right\}\mathbf{B}\end{aligned} \tag{19}$$

and $\mathbf{E}=\mathbf{A}\mathbf{\Sigma}\mathbf{B}$ denotes the SVD of $\mathbf{E}\in\Re^{n_3\times n_1n_2}$, and $\delta_j$ denotes the $j$th singular value of $\mathbf{E}$.

Thus, we can further obtain $\mathcal{L}^{(i+1)}$ by the mode-3 folding operation as

$$\mathcal{L}^{(i+1)}=\mathrm{fold}_3\left(\mathrm{unfold}_3(\mathcal{L}^{(i+1)})\right). \tag{20}$$

*3) Optimization of $\mathcal{W}_k$, $(k=1,2)$:* The subproblem of $\mathcal{W}_k^{(i+1)}$, $(k=1,2)$ is given as

$$\min_{\mathcal{W}_k}\frac{\mu_k}{2}\left\|\mathcal{W}_k-\nabla_k\mathcal{X}^{(i)}-\mathcal{H}_k^{(i)}\right\|_F^2+\alpha_k\|\mathcal{W}_k\|_{\mathrm{TNN}_k}. \tag{21}$$

According to [49], by using the mode-$k$ TNN-based tensor singular value thresholding (t-SVT) method, the $\mathcal{W}_k^{(i+1)}$ subproblem can be efficiently solved by

$$\mathcal{W}_k^{(i+1)}=\mathcal{D}_{\mathrm{TNN}_k}^{\alpha_k/\mu_k}\left(\nabla_k\mathcal{X}^{(i)}+\mathcal{H}_k^{(i)}\right). \tag{22}$$

*4) Optimization of $\mathcal{X}$:* The subproblem of $\mathcal{X}^{(i+1)}$ is given as

$$\begin{aligned}\min_{\mathcal{X}}\ &\tfrac{1}{2}\left\|\mathcal{Y}-\mathcal{X}-\mathcal{S}^{(i+1)}\right\|_F^2+\tfrac{\eta}{2}\left\|\mathcal{L}^{(i+1)}-\nabla_3\mathcal{X}-\mathcal{U}^{(i)}\right\|_F^2\\ &+\sum_{k=1}^{2}\tfrac{\mu_k}{2}\left\|\mathcal{W}_k^{(i+1)}-\nabla_k\mathcal{X}-\mathcal{H}_k^{(i)}\right\|_F^2.\end{aligned} \tag{23}$$

Specifically, $\mathcal{X}^{(i+1)}$ subproblem (23) can be efficiently solved by the fast Fourier transform (FFT) as

$$\mathcal{X}^{(i+1)}=\mathcal{F}^{-1}\times\left(\frac{\mathcal{F}(\mathcal{A})+\sum_{k=1}^{2}\mu_k\mathcal{F}(\nabla_k)^{\mathrm{H}}\mathcal{F}(\mathcal{B})+\eta\mathcal{F}(\nabla_3)^{\mathrm{H}}\mathcal{F}(\mathcal{C})}{1+\sum_{k=1}^{2}\mu_k\mathcal{F}(\nabla_k)^{\mathrm{H}}\mathcal{F}(\nabla_k)+\eta\mathcal{F}(\nabla_3)^{\mathrm{H}}\mathcal{F}(\nabla_3)}\right) \tag{24}$$

where $\mathcal{A}=\mathcal{Y}-\mathcal{S}^{(i+1)}$, $\mathcal{B}=\mathcal{W}_k^{(i+1)}-\mathcal{H}_k^{(i)}$, $\mathcal{C}=\mathcal{L}^{(i+1)}-\mathcal{U}^{(i)}$, $\mathcal{F}(\cdot)$, and $\mathcal{F}^{-1}(\cdot)$ are the FFT and inverse FFT operators, respectively, and $(\cdot)^{\mathrm{H}}$ denotes the complex conjugate operator.

**Algorithm 1:** Algorithm for Tensor-Based HSI Restoration Model With Low-Rank Modeling in Gradient Domains.

**Input**: noisy HSI $\mathcal{Y}\in\Re^{n_1\times n_2\times n_3}$, and parameters $\lambda_1,\lambda_2,\eta,\alpha_1,\alpha_2,\mu_1,\mu_2,MaxIter$.
**Initialization**: $i=0$,
$\mathcal{X}^{(0)}=\mathcal{S}^{(0)}=\mathcal{L}^{(0)}=\mathcal{U}^{(0)}=0$,
$\mathcal{W}_1^{(0)}=\mathcal{W}_2^{(0)}=\mathcal{H}_1^{(0)}=\mathcal{H}_2^{(0)}=0$.
**Iterations**:
  **For** $i=0$ **to** $MaxIter-1$ **Do**
    Solve $\mathcal{S}^{(i+1)}$ via (15);
    Solve $\mathcal{L}^{(i+1)}$ via (18) and (20);
    Solve $\mathcal{W}_1^{(i+1)}$ and $\mathcal{W}_2^{(i+1)}$ via (22);
    Solve $\mathcal{X}^{(i+1)}$ via (24);
    Update $\mathcal{U}^{(i+1)}$, $\mathcal{H}_1^{(i+1)}$ and $\mathcal{H}_2^{(i+1)}$ via (25);
  **End For**
**Output**: the restored HSI $\mathcal{X}^{(MaxIter)}$.

*5) Update $\mathcal{U}$ and $\mathcal{H}_k$, $(k=1,2)$:* Finally, the Lagrange multipliers $\mathcal{U}$ and $\mathcal{H}_k$, $(k=1,2)$ are updated as

$$\begin{cases}\mathcal{U}^{(i+1)}=\mathcal{U}^{(i)}+\nabla_3\mathcal{X}^{(i+1)}-\mathcal{L}^{(i+1)}\\ \mathcal{H}_k^{(i+1)}=\mathcal{H}_k^{(i)}+\nabla_k\mathcal{X}^{(i+1)}-\mathcal{W}_k^{(i+1)}.\end{cases} \tag{25}$$

Thus, the whole optimization of the proposed tensor-based HSI restoration model with low-rank modeling in gradient domains (11) is given in Algorithm 1.

## IV. Experiments

### A. Experiment Setting

In order to verify the effectiveness of our proposed tensor-based HSI restoration method with low-rank modeling in gradient domains, we have carried out many denoising experiments on various simulated and real HSI datasets by comparing with some state-of-the-art methods. In this article, two simulated datasets and three real datasets are used for the HSI denoising experiments.

Moreover, we clearly compared the proposed method with some state-of-the-art denoising methods, such as LRMR [19], LRTV [30], LRTDTV [34], 3DTNN [49], LRTFDFR [35], intrinsic tensor sparsity regularization (ITSR) [60], nonlocal meets global (NG-meet) [61], FGSLR$_{1/2}$ [51], and HSID-CNN [56]. In order to comprehensively evaluate the performance of different denoising methods, visual comparison and quantitative comparison are both analyzed.

All the experiments are carried out on Windows 11 and MATLAB(R2016a), which uses Intel Core i5-10210 U 1.6 GHz and 16 GB RAM.

### B. Experiments With Simulated Datasets

In this section, the visually and quantitatively experimental results of simulated HSI datasets are clearly given.

*1) Description of the Simulated Datasets:* For the simulated HSI datasets, we apply a subcube with size $200\times200\times80$ of Pavia City Center (PaviaC) dataset and a subcube with

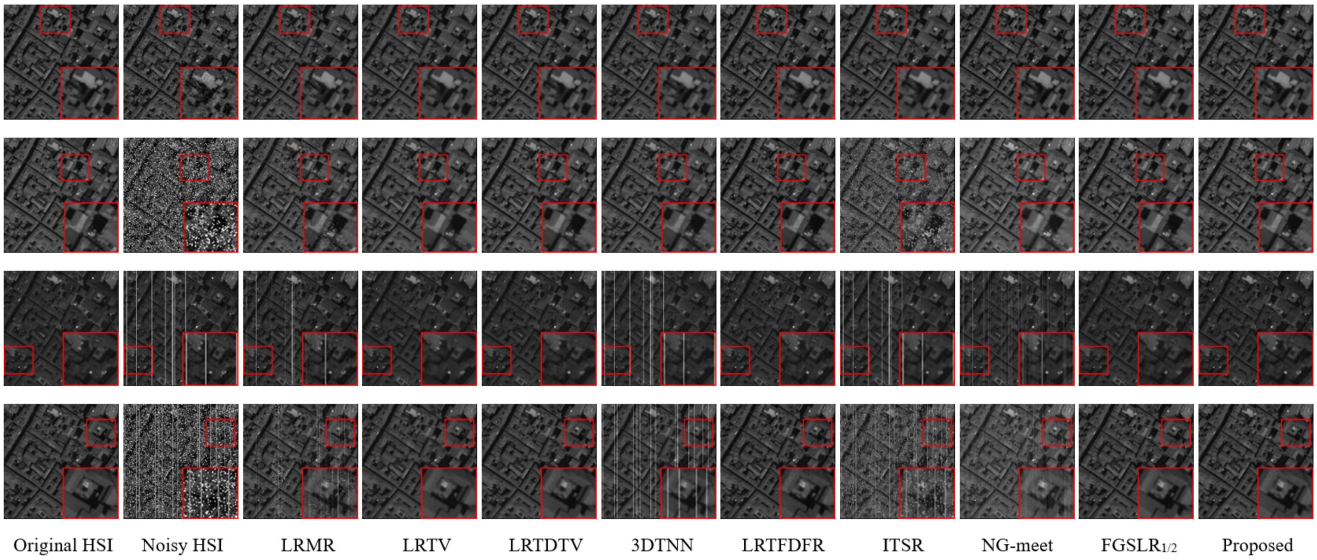


Fig. 2. Denoising results of different methods on different bands of the simulated PaviaC dataset under different noise cases. (From Top-row to Bottom-row): Results of band 41 under Case 1, Results of band 49 under Case 2, Results of band 1 under Case 4, Results of band 30 under Case 6. (From Left-column to Right-column): Results of Original HSI, Noisy HSI, LRMR, LRTV, LRTDTV, 3DTNN, LRTFDFR, ITSR, NG-meet, FGSLR$_{1/2}$, and Proposed.

size $256 \times 256 \times 191$ of Washington DC Mall (WDC) dataset. Then, three quantitative image quality indexes, namely, the mean peak signal-to-noise ratio (MPSNR), mean structural similarity (MSSIM), and spectral angle mapper (SAM) are used to evaluate the quality of denoised HSIs.

Specifically, we add six cases of different noise to the clean HSI to generate the simulated PaviaC and WDC datasets, which are the following six cases.

*Case 1: (Gaussian Noise)* Zero-mean Gaussian noise with different signal-to-noise ratio randomly selected between 10 and 20 dB is added to each band of the PaviaC and WDC dataset.

*Case 2: (Gaussian Noise + Salt and Pepper)* Gaussian noise is added in the same way as Case 1, and then the salt and pepper noise with a density of 20 is randomly added to 20 bands.

*Case 3: (Gaussian Noise + Deadlines)* Add Gaussian noise in the same way as Case 1, and then randomly select 10 bands to add the deadlines.

*Case 4: (Gaussian Noise + Stripes)* Gaussian noise is added in the same way as Case 1, and then 20 bands are randomly selected to add the stripes, where the number of stripes added in each band is randomly selected from the integer set of $\{6, 7, \ldots, 14, 15\}$.

*Case 5: (Gaussian Noise + Salt and Pepper + Deadlines)* Gaussian noise and salt and pepper noise are added in the same way as Case 2, and then the deadlines are added into the ten bands, where five bands are randomly selected from the 20 bands containing salt and pepper noise, and the rest five bands are randomly selected from the other bands.

*Case 6: (Gaussian Noise + Salt and Pepper + Deadlines + Stripes)* Gaussian noise, impulse noise, and deadlines are added in the same way as Case 5, and then the stripes are added in 20 bands containing salt and pepper noise, where the number of stripes added in each band is randomly selected from the integer set of $\{6, 7, \ldots, 14, 15\}$.

*2) Comparisons With Different Methods:* More clearly, for the simulated data experiments, the representative results of Case 1, Case 2, Case 4, and Case 6 are selected to evaluate the visual performance of different denoising methods. Thus, Figs. 2 and 3 showed the visual denoising results of different methods on different bands of the two simulated PaviaC and WDC datasets under the above four noise cases, respectively. Meanwhile, in order to better observe and compare the local details of the images in Figs. 2 and 3, the area depicted by the red rectangle in the local area is enlarged in the right-bottom area.

Specifically, Fig. 2 shows the denoising results of all methods on the given band 41, band 49, band 1, and band 30 of the simulated PaviaC dataset under Case 1, Case 2, Case 4, and Case 6, respectively.

As shown in the top-row of Fig. 2, i.e., band 41 of the simulated PaviaC dataset under Case 1 with Gaussian noise, all the methods can effectively remove the Gaussian noise, but LRMR, LRTV, LRTDTV, 3DTNN, LRTFDFR, ITSR, and NG-meet methods more or less blur the details of the image. Moreover, FGSLR$_{1/2}$ and the proposed method restore the original clean image to the greatest extent while better preserving the image details and structures.

As shown in the second-row of Fig. 2, i.e., band 49 of the simulated PaviaC dataset under Case 2 with Gaussian and Salt and Pepper Noise, we can clearly see that ITSR can not effectively remove the noise, and LRMR still has a small amount of noise. LRTV, LRTDTV, 3DTNN, LRTFDFR, NG-meet, and FGSLR$_{1/2}$ can well remove the noise, but still have some shortcomings in preserving the image details, which slightly blur few details of the image at different degrees. By contrast, the proposed method shows better denoising performance, which can better remove the noise and at the same time restore the image texture structure and details finer.

As shown in the third-row of Fig. 2, i.e., band 1 of the simulated PaviaC dataset under Case 4 with Gaussian Noise and Stripes, LRMR, 3DTNN, ITSR, and NG-meet can not

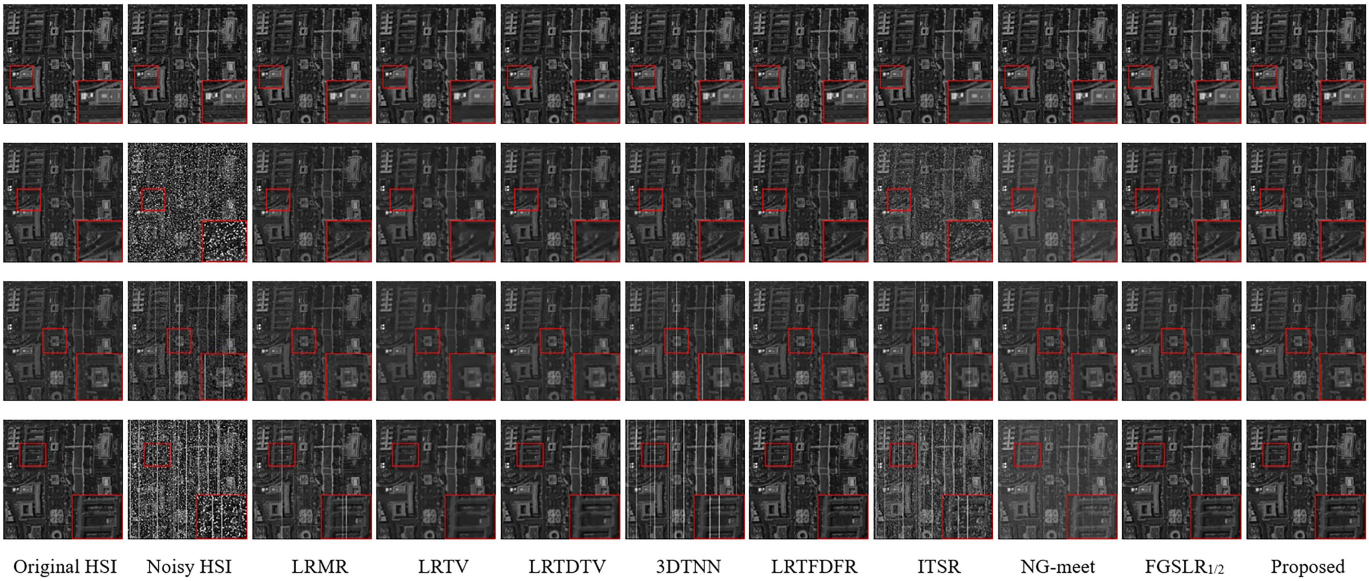


Fig. 3. Denoising results of different methods on different bands of the simulated WDC dataset under different noise cases. (From Top-row to Bottom-row): Results of band 43 under Case 1, Results of band 31 under Case 2, Results of band 22 under Case 4, Results of band 37 under Case 6. (From Left-column to Right-column): Results of original HSI, Noisy HSI, LRMR, LRTV, LRTDTV, 3DTNN, LRTFDFR, ITSR, NG-meet, FGSLR$_{1/2}$, and proposed.

effectively remove the stripe noise, whereas LRTV, LRTDTV, and LRTFDFR can well remove the stripe noise, but still blur some image details at different degrees. The denoising result of FGSLR$_{1/2}$ is satisfactory, but a few local details are not well preserved in the enlarged region. What is more, the proposed method performs much better results in removing stripe noise and preserving image details.

As shown in the bottom-row of Fig. 2, i.e., band 30 of the simulated PaviaC dataset under Case 6 with Gaussian noise, salt and pepper, deadlines, and stripes, four kinds of mixed noise are added to the original image to generate the simulated noisy image. However, the mixed noise can not be effectively removed by LRMR, 3DTNN, ITSR, and NG-meet, and their restored results are not satisfactory. Specifically, LRMR, 3DTNN, ITSR, and NG-meet can not well remove the stripe and deadline noise. LRTV, LRTDTV, and LRTFDFR can well remove the stripe and deadline noise, and they also have some information loss and blur artifacts at different degrees. FGSLR$_{1/2}$ can obtain very satisfactory restored result. Compared with other methods, the proposed method achieves the best visual performance, which can best remove the stripe and deadline noise, and also preserve the image details finest.

Furthermore, Fig. 3 shows the denoising results on the given band 43, band 31, band 22, and band 37 of the simulated WDC dataset under Case 1, Case 2, Case 4, and Case 6, respectively.

As shown in the top-row of Fig. 3, i.e., band 43 of the simulated WDC dataset under Case 1 with Gaussian noise, all the methods can well remove the Gaussian noise. Meanwhile, the results of LRTV, LRTDTV, and ITSR are too smooth. LRMR, 3DTNN, LRTFDFR, NG-meet, and FGSLR$_{1/2}$ all have the problem of loss of image details in different degrees. The proposed method can better preserve the global and local details of the image, and has the best visual effect.

As shown in the second-row of Fig. 3, i.e., band 31 of the simulated WDC dataset under Case 2 with Gaussian and Salt and Pepper Noise, the image restored by ITSR still contains a small amount of noise. LRTV and LRTDTV blur more details of image, LRMR, 3DTNN, LRTFDFR, and NG-meet blur less details of image. The denoising result of FGSLR$_{1/2}$ is satisfactory, but it can be seen from the enlarged region that the details of the image are also slightly blurred. Moreover, the proposed method shows better results in removing noise and preserving details.

As shown in the third-row of Fig. 3, i.e., band 22 of the simulated WDC dataset under Case 4 with Gaussian Noise and Stripes, 3DTNN and ITSR can not well remove the stripes, and the denoising results of LRTV and LRTDTV are not very ideal, thus losing some image details. LRMR, LRTFDFR, NG-meet, FGSLR$_{1/2}$ and the proposed method show good performance in removing the stripes, and the image recovered by the proposed method is the closest to the original HSI.

As shown in the bottom-row of Fig. 3, i.e., band 37 of the simulated WDC dataset under Case 6 with Gaussian noise, salt and pepper, deadlines, and stripes, ITSR only removes a small portion of the noise. Moreover, ITSR and 3DTNN can not well remove the deadlines, and stripes, and LRMR and NG-meet can remove some deadlines and stripes but also remain few stripes in the denoised images with a much closer look. LRTV, LRTDTV, LRTFDFR, and FGSLR$_{1/2}$ can well remove the deadlines and stripes, thus showing satisfactory results. Clearly, the visual performance of the proposed method is the most satisfactory, which can best remove the stripe and deadline noise, and preserve image details at the same time.

In summary, for above visual comparisons of different cases of two simulated PaviaC and WDC datasets, the denoising results of our proposed method are still excellent. In all cases, it can well remove the mixed noise, restore the clean image, and preserve the original information of the image. With the variety of mixed noise added, the superiority of the proposed method is more obvious and robust in removing the deadlines and stripes.

TABLE II
MPSNR, MSSIM, AND SAM VALUES OF DIFFERENT METHODS ON THE SIMULATED PAVIAC DATASET

| Case | Index | LRMR | LRTV | LRTDTV | 3DTNN | LRTFDFR | ITSR | NG-meet | FGSLR$_{1/2}$ | Proposed |
|---|---|---|---|---|---|---|---|---|---|---|
| **Case 1** | MPSNR | 37.58 | 35.31 | 36.34 | 36.66 | 37.96 | 36.25 | 39.33 | 39.62 | **40.66** |
| | MSSIM | 0.9668 | 0.9347 | 0.9627 | 0.9766 | 0.9426 | 0.9616 | 0.9648 | 0.9831 | **0.9849** |
| | SAM | 4.1048 | 5.9083 | 2.9788 | 2.2096 | 7.0639 | 2.4630 | 5.3219 | 2.1726 | **2.1228** |
| **Case 2** | MPSNR | 33.77 | 34.38 | 35.84 | 36.06 | 35.62 | 30.37 | 30.08 | 38.95 | **39.27** |
| | MSSIM | 0.9157 | 0.9108 | 0.9556 | 0.9732 | 0.8983 | 0.8090 | 0.8786 | 0.9806 | **0.9827** |
| | SAM | 10.6513 | 10.4936 | 3.4946 | 2.3474 | 16.9773 | 13.7567 | 11.0469 | 2.2106 | **2.1701** |
| **Case 3** | MPSNR | 34.35 | 32.69 | 33.75 | 33.93 | 34.55 | 33.20 | 36.11 | 36.78 | **39.62** |
| | MSSIM | 0.9245 | 0.9013 | 0.9231 | 0.9334 | 0.9022 | 0.9164 | 0.9276 | 0.9415 | **0.9806** |
| | SAM | 5.7851 | 6.4856 | 4.6079 | 4.1496 | 8.2758 | 4.4450 | 6.0285 | 3.9563 | **2.2460** |
| **Case 4** | MPSNR | 34.25 | 35.21 | 36.07 | 32.73 | 37.57 | 31.25 | 34.78 | 38.75 | **40.54** |
| | MSSIM | 0.9422 | 0.9328 | 0.9582 | 0.9220 | 0.9404 | 0.8980 | 0.9257 | 0.9808 | **0.9856** |
| | SAM | 6.6022 | 6.4914 | 3.5676 | 9.4089 | 8.0483 | 9.5031 | 6.6628 | 2.2627 | **2.0772** |
| **Case 5** | MPSNR | 32.10 | 31.87 | 33.27 | 33.64 | 33.06 | 29.09 | 28.45 | 36.70 | **38.27** |
| | MSSIM | 0.8880 | 0.8745 | 0.9180 | 0.9363 | 0.8660 | 0.7934 | 0.8486 | 0.9668 | **0.9746** |
| | SAM | 14.2108 | 14.1966 | 5.8345 | 4.3309 | 18.2277 | 15.0007 | 13.6883 | 3.1447 | **2.5769** |
| **Case 6** | MPSNR | 30.99 | 32.83 | 33.68 | 31.02 | 32.24 | 28.26 | 27.14 | 36.65 | **38.68** |
| | MSSIM | 0.8622 | 0.8809 | 0.9155 | 0.8797 | 0.8456 | 0.7588 | 0.8152 | 0.9408 | **0.9789** |
| | SAM | 11.5738 | 11.8833 | 5.7710 | 11.5004 | 19.8349 | 16.9168 | 12.7485 | 3.9422 | **2.2321** |

TABLE III
MPSNR, MSSIM, AND SAM VALUES OF DIFFERENT METHODS ON THE SIMULATED WDC DATASET

| Case | Index | LRMR | LRTV | LRTDTV | 3DTNN | LRTFDFR | ITSR | NG-meet | FGSLR$_{1/2}$ | Proposed |
|---|---|---|---|---|---|---|---|---|---|---|
| **Case 1** | MPSNR | 38.47 | 33.07 | 33.98 | 38.26 | 38.91 | 37.20 | 38.67 | 39.12 | **39.46** |
| | MSSIM | 0.9910 | 0.9738 | 0.9811 | 0.9920 | 0.9856 | 0.9697 | 0.9796 | 0.9799 | **0.9934** |
| | SAM | 3.7381 | 4.9395 | 3.9049 | **2.6269** | 6.4111 | 2.8489 | 3.1090 | 2.8682 | 3.4275 |
| **Case 2** | MPSNR | 37.47 | 33.06 | 33.97 | 38.11 | 38.27 | 33.65 | 33.24 | 38.79 | **39.29** |
| | MSSIM | 0.9817 | 0.9710 | 0.9810 | 0.9917 | 0.9827 | 0.8972 | 0.9353 | 0.9787 | **0.9925** |
| | SAM | 6.2301 | 5.1313 | 3.9248 | **2.6761** | 7.3175 | 11.0557 | 10.0347 | 2.9928 | 3.6029 |
| **Case 3** | MPSNR | 37.60 | 32.56 | 33.16 | 37.22 | 37.88 | 36.08 | 37.82 | 39.26 | **39.45** |
| | MSSIM | 0.9636 | 0.9034 | 0.9243 | 0.9718 | 0.9553 | 0.9583 | 0.9727 | 0.9735 | **0.9806** |
| | SAM | 4.7632 | 5.1643 | 4.8885 | 3.8424 | 6.4516 | 4.0736 | 3.9198 | 3.7746 | **3.3613** |
| **Case 4** | MPSNR | 38.21 | 33.31 | 33.91 | 36.71 | 38.98 | 35.01 | 37.18 | 39.16 | **39.88** |
| | MSSIM | 0.9726 | 0.9108 | 0.9327 | 0.9650 | 0.9663 | 0.9467 | 0.9716 | 0.9800 | **0.9807** |
| | SAM | 3.8378 | 4.6393 | 4.3410 | 6.8268 | 5.7671 | 6.3903 | 4.5229 | **2.7643** | 3.2680 |
| **Case 5** | MPSNR | 36.55 | 32.36 | 33.20 | 37.14 | 37.45 | 32.82 | 32.64 | 39.28 | **39.39** |
| | MSSIM | 0.9484 | 0.8931 | 0.9221 | 0.9693 | 0.9449 | 0.8841 | 0.9206 | 0.9713 | **0.9775** |
| | SAM | 6.7775 | 6.9544 | 4.7923 | 3.8073 | 11.0530 | 11.9248 | 10.0715 | 3.7672 | **3.4073** |
| **Case 6** | MPSNR | 35.85 | 32.16 | 32.89 | 35.79 | 37.21 | 32.73 | 32.38 | 38.88 | **39.33** |
| | MSSIM | 0.9399 | 0.8878 | 0.9176 | 0.9468 | 0.9429 | 0.8824 | 0.9120 | 0.9589 | **0.9752** |
| | SAM | 8.5104 | 8.5693 | 5.7318 | 9.0549 | 11.1079 | 14.0402 | 12.6967 | 8.7594 | **3.5135** |

Clearly, for the quantitative evaluation of different methods, Tables II and III give the quantitative MPSNR, MSSIM, and SAM results of different methods on the simulated PaviaC and WDC datasets under different noise cases, respectively. Moreover, in Tables II and III, the best results of each quality index are shown in bold, and the second best results are shown in underline.

As shown in Table II, the MPSNR, MSSIM, and SAM values of the proposed method are the best for all these six cases, which thus show that the proposed method achieves the best denoising results on the simulated PaviaC dataset.

As shown in Table III, the proposed method achieves the best results for most of the cases. Clearly, the proposed method gives the best MPSNR and MSSIM results for Case 1, Case 2, and Case 4, and the second best SAM result for Case 4, where 3DTNN gives the best SAM results for Case 1 and Case 2, and FGSLR$_{1/2}$ gives the best SAM result for Case 4. What is more, the proposed method consistently gives the best MPSNR, MSSIM, and SAM

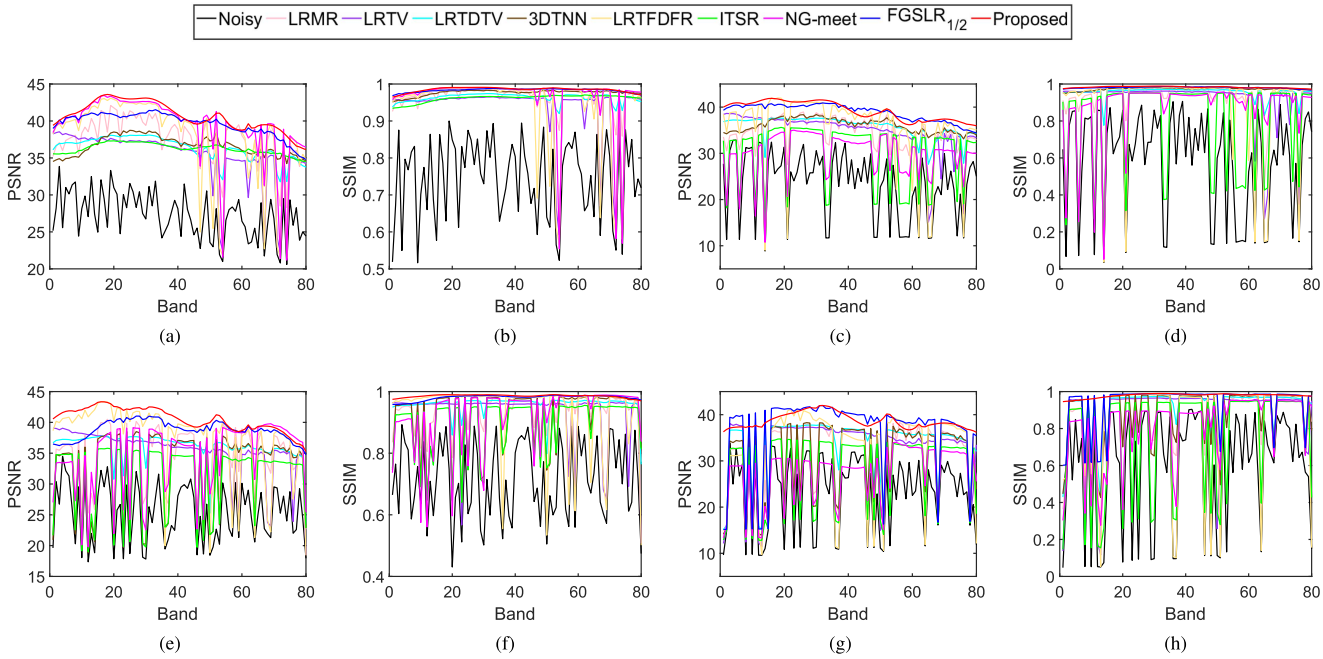


Fig. 4. PSNR and SSIM values in each band of different methods on the simulated PaviaC dataset under different noise cases. (a) PSNR under Case 1. (b) SSIM under Case 1. (c) PSNR under Case 2. (d) SSIM under Case 2. (e) PSNR under Case 4. (f) SSIM under Case 4. (g) PSNR under Case 6. (h) SSIM under Case 6.

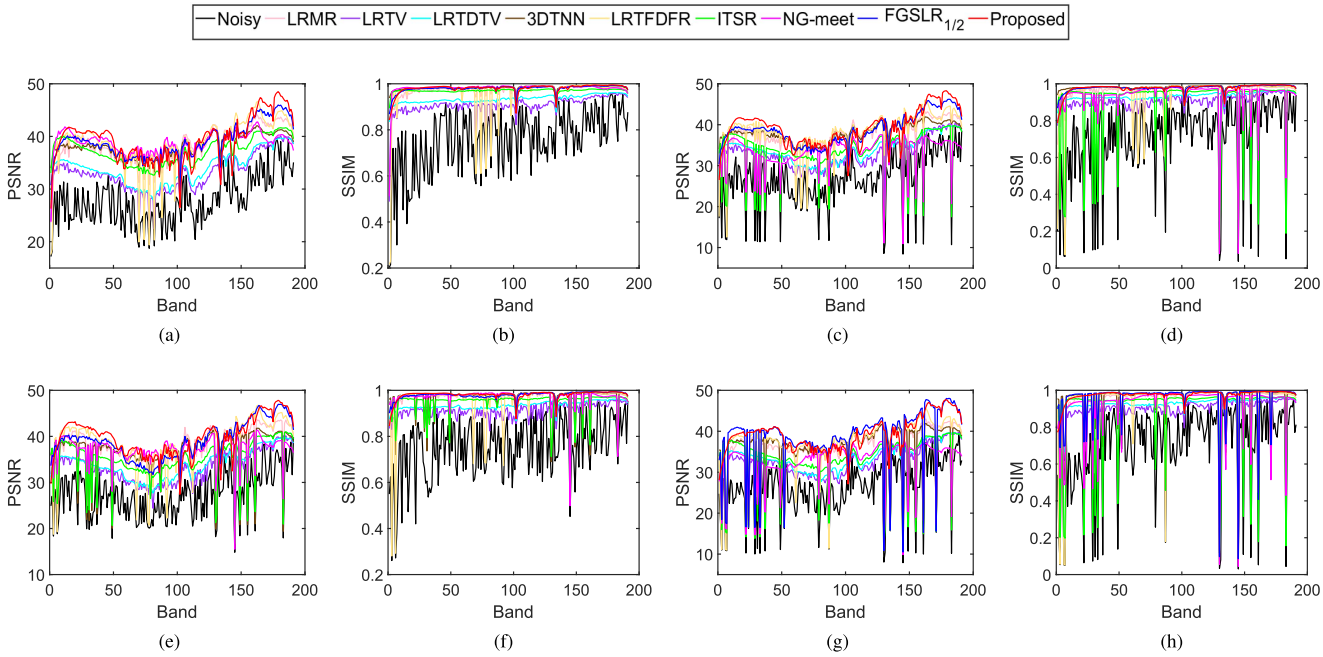


Fig. 5. PSNR and SSIM values in each band of different methods on the simulated WDC dataset under different noise cases. (a) PSNR under Case 1. (b) SSIM under Case 1. (c) PSNR under Case 2. (d) SSIM under Case 2. (e) PSNR under Case 4. (f) SSIM under Case 4. (g) PSNR under Case 6. (h) SSIM under Case 6.

results for the rest Case 3, Case 5, and Case 6. Moreover, in most cases of the simulated WDC dataset, the proposed method is much better than the other compared methods.

More specifically, Figs. 4 and 5 show the PSNR and SSIM values of each band of different methods on the simulated PaviaC and WDC datasets under Case 1, Case 2, Case 4, and Case 6, respectively. It can be seen from Figs. 4 and 5 that the proposed method achieves the best PSNR and SSIM values in most bands of the simulated PaviaC and WDC datasets. It is worth noting that the curves of PSNR and SSIM of the proposed method are smooth and stable, while the other methods cause the large fluctuations owing to the deadlines or stripes noise at these bands are not well removed. Therefore, the proposed method has better denoising ability to remove deadlines and stripes in mixed noise.

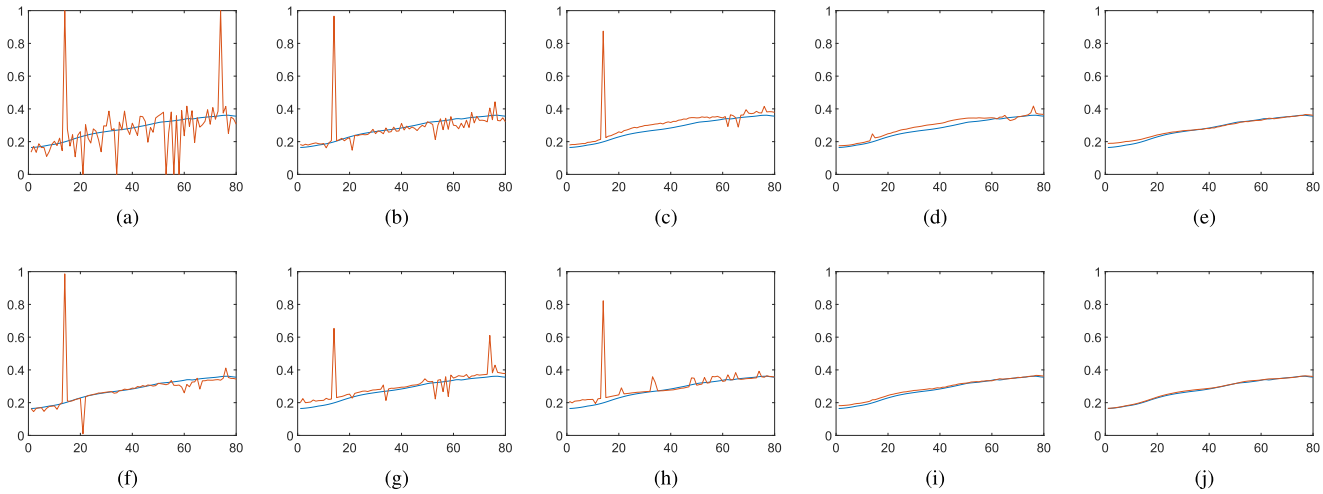


Fig. 6. Comparisons of the spectrum of different methods on the simulated PaviaC dataset under Case 2 at spatial position (10,69), where the *blue* color denotes the spectrum of Original HSI. (a) Noisy HSI. (b) LRMR. (c) LRTV. (d) LRTDTV. (e) 3DTNN. (f) LRTFDFR. (g) ITSR. (h) NG-meet. (i) FGSLR$_{1/2}$. (j) Proposed.

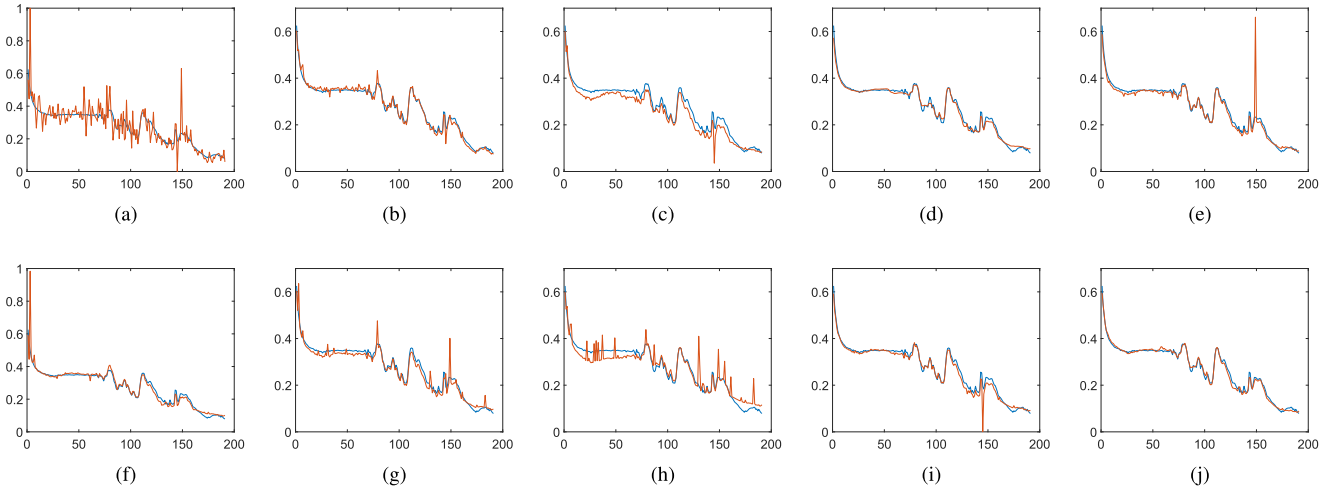


Fig. 7. Comparisons of the spectrum of different methods on the simulated WDC dataset under Case 6 at spatial position (30,30), where the *blue* color denotes the spectrum of Original HSI. (a) Noisy HSI. (b) LRMR. (c) LRTV. (d) LRTDTV. (e) 3DTNN. (f) LRTFDFR. (g) ITSR. (h) NG-meet. (i) FGSLR$_{1/2}$. (j) Proposed.

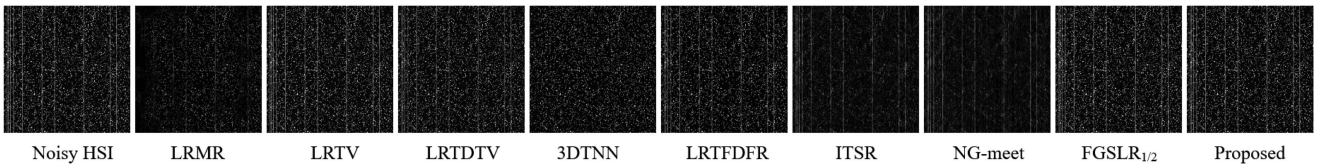


Fig. 8. Comparisons of the sparse noise $\mathcal{S}$ of different methods on band 37 of the simulated PaviaC dataset under Case 6. (From Left to Right): Results of the sparse noise $\mathcal{S}$ of Noisy HSI, LRMR, LRTV, LRTDTV, 3DTNN, LRTFDFR, ITSR, NG-meet, FGSLR$_{1/2}$, and proposed.

In general, by comparing with the other methods on the simulated PaviaC and WDC datasets, the proposed method has advantages in both visual evaluation and quantitative evaluation. Thus, it further proves that the proposed method is more effective and feasible for removing mixed noise of HSI.

*3) Comparisons of Spectrum Preserving of Different Methods:* Moreover, we further compare the results of preserving the spectrum of HSI of different methods. Thus, Figs. 6 and 7 particularly show the restored spectrum of different methods on the simulated PaviaC dataset under Case 2 at spatial position (10,69), and the simulated WDC dataset under Case 6 at spatial position (30,30), respectively. As clearly displayed in Figs. 6 and 7, the proposed method can best restore and preserve the spectrum of original HSI, which are closest to the spectrum of original HSI marked by the blue curve.

*4) Comparisons of the Sparse Noise $\mathcal{S}$ Restored by Different Methods:* Furthermore, we also analyze the results of sparse noise $\mathcal{S}$ restored by different methods. To this end, Figs. 8 and 9 particularly display the results of sparse noise $\mathcal{S}$ restored by different methods on the band 37 of simulated PaviaC dataset

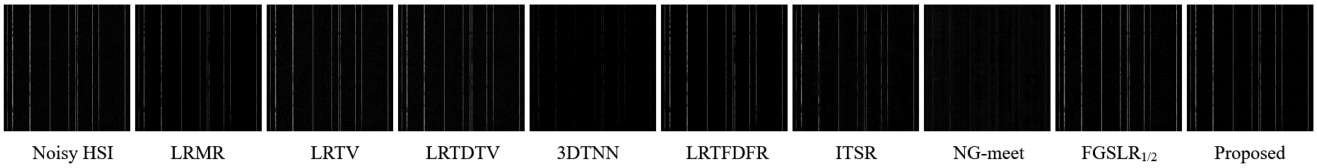


Fig. 9. Comparisons of the sparse noise $\mathcal{S}$ of different methods on band 49 of the simulated WDC dataset under Case 4. (From Left to Right): Results of the sparse noise $\mathcal{S}$ of noisy HSI, LRMR, LRTV, LRTDTV, 3DTNN, LRTFDFR, ITSR, NG-meet, FGSLR$_{1/2}$, and proposed.

TABLE IV
MPSNR, MSSIM, AND SAM VALUES OF HSID-CNN AND THE PROPOSED METHOD ON THE SIMULATED PAVIAC DATASET WITH THE GAUSSIAN NOISE OF DIFFERENT LEVELS

| Gaussian noise level | Index | Noisy | HSID-CNN | Proposed |
|---|---|---|---|---|
| $\sigma_n = 5$ | MPSNR | 34.15 | 44.05 | **45.60** |
| | MSSIM | 0.9308 | 0.9930 | **0.9956** |
| | SAM | 5.7042 | 1.7017 | **1.2258** |
| $\sigma_n = 25$ | MPSNR | 20.18 | 34.35 | **35.19** |
| | MSSIM | 0.4295 | 0.9440 | **0.9493** |
| | SAM | 25.0387 | 3.4700 | **3.4418** |
| $\sigma_n = 50$ | MPSNR | 14.15 | 31.38 | **31.44** |
| | MSSIM | 0.1788 | **0.8950** | 0.8903 |
| | SAM | 41.2716 | 5.8128 | **4.9031** |
| $\sigma_n = 75$ | MPSNR | 10.63 | 29.39 | **29.45** |
| | MSSIM | 0.0912 | **0.8410** | 0.8395 |
| | SAM | 51.8654 | 6.9241 | **5.8062** |
| $\sigma_n = 100$ | MPSNR | 8.14 | **28.28** | 28.24 |
| | MSSIM | 0.0532 | 0.8047 | **0.8110** |
| | SAM | 58.9691 | 7.3428 | **5.9397** |

under Case 6, and the band 49 of simulated WDC dataset under Case 4, respectively. As clearly displayed in Figs. 8 and 9, by comparing with the sparse noise $\mathcal{S}$ of noisy HSI, (i.e., the original sparse noise $\mathcal{S}$ as reference), the proposed method can best restore the sparse noise $\mathcal{S}$ among these compared methods.

*5) Comparison With Deep Learning Method:* Moreover, to further illustrate the effectiveness of the proposed method against the deep learning method, we also compare our proposed method with the HSID-CNN method [56]. As we clearly know, the HSID-CNN method is just proposed for the additive Gaussian noise removal from HSIs [56]. Thus, to make the comparison more fair, we particularly use the aforementioned simulated PaviaC dataset of size $200 \times 200 \times 80$ with the additive Gaussian noise of five different variances $\sigma_n^2$, i.e., $\sigma_n = 5$, $\sigma_n = 25$, $\sigma_n = 50$, $\sigma_n = 75$, and $\sigma_n = 100$, which are the same as the simulated experiments conducted by the HSID-CNN method. In this sense, we give the correspondingly quantitative results in Table IV. Clearly, our proposed method gives better MPSNR, MSSIM, and SAM results than those of HSID-CNN for most of the cases, which shows that our proposed method can give better denoising performance than HSID-CNN generally.

### C. Experiments With Real Datasets

In this section, the experimental results of real HSI datasets are also given.

For the real HSI datasets, we apply a subcube with size $207 \times 207 \times 210$ of HYDICE Urban (Urban) dataset, a subcube with size $200 \times 200 \times 166$ of EO-1 Hyperion (EO-1) dataset [19],[30], and the Pavia University (PaviaU) dataset with size $610 \times 340 \times 103$.

Moreover, the denoising results of different methods on the real Urban, EO-1, and PaviaU datasets are shown in Figs. 10–12, respectively.

As shown in Fig. 10, i.e., band 108 of the real Urban dataset, it is obvious that the original band 108 of Urban is very blurred after being polluted by the noise. From the whole parts and the red enlarged parts of the denoised images, we can clearly see that LRMR and LRTFDFR have only removed a little amount of noise, and their denoised images are still blurred. LRTV, LRTDTV, 3DTNN, ITSR, NG-meet, and FGSLR$_{1/2}$ remove more of the noise, and the objects in the red box become also visible. However, compared with the proposed method, the restored results of the LRTV, LRTDTV, 3DTNN, ITSR, NG-meet, and FGSLR$_{1/2}$ methods are still not satisfied, which also lose many image details. More clearly, the proposed method can best remove the noise and preserve image details. Therefore, the proposed method shows the best visual denoising performance on the real Urban dataset.

Then, Fig. 11 shows the denoising results of the band 95 of the real EO-1 dataset. From the whole parts and the enlarged red box of the images, we can clearly see that the denoising performance of LRMR, LRTV, and LRTFDFR on the real EO-1 dataset is not ideal, and their restored images are still blurred and noisy. LRTDTV, 3DTNN, ITSR, NG-meet, and FGSLR$_{1/2}$ can remove more of the noise. However, by comparing with the proposed method, LRTDTV, 3DTNN, ITSR, NG-meet, and FGSLR$_{1/2}$ can not well preserve the details of the image, which are also some blurred and are not as fine as the restored image of the proposed method. Clearly, the proposed method can best remove the noise and preserve image details finest. Therefore, the denoising performance of the proposed method on the real EO-1 dataset is the best.

Moreover, Fig. 12 shows the denoising results of the band 3 of the real PaviaU dataset, where the denoising performance of each method is similar with the cases of real Urban and EO-1 datasets.

Meanwhile, we use the no-reference HSI quality assessment (NHSIQA) index [62] for quantitatively assessing the real data denoising experiments. Then, Table V gives the NHSIQA results of different approaches on the real Urban, EO-1, and PaviaU datasets, where the smaller NHSIQA stands for the higher quality of HSI. As given in Table V, the proposed approach consistently gives the smallest NHSIQA results, i.e., the highest quality of restored HSI.

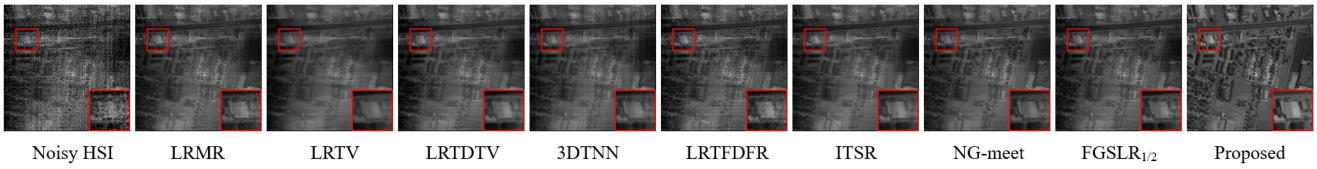


Fig. 10. Denoising results of different methods on band 108 of the real Urban dataset. (From left to Right): Results of Noisy HSI, LRMR, LRTV, LRTDTV, 3DTNN, LRTFDFR, ITSR, NG-meet, FGSLR$_{1/2}$, and proposed.

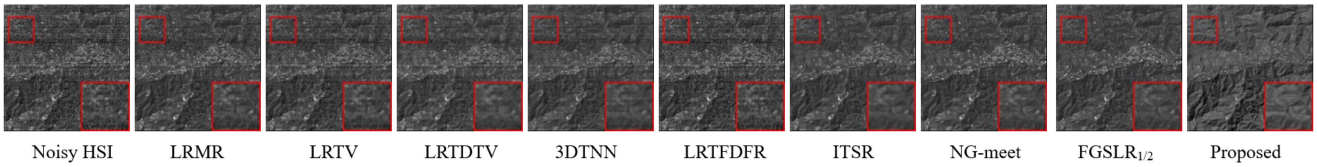


Fig. 11. Denoising results of different methods on band 95 of the real EO-1 dataset. (From Left to Right): Results of Noisy HSI, LRMR, LRTV, LRTDTV, 3DTNN, LRTFDFR, ITSR, NG-meet, FGSLR$_{1/2}$, and proposed.


Fig. 12. Denoising results of different methods on band 3 of the real PaviaU dataset. (From Left to Right): Results of noisy HSI, LRMR, LRTV, LRTDTV, 3DTNN, LRTFDFR, ITSR, NG-meet, FGSLR$_{1/2}$, and proposed.

TABLE V
NO-REFERENCE HSI QUALITY ASSESSMENT (NHSIQA) VALUES OF DIFFERENT METHODS ON THE REAL HSI DATASETS

| | LRMR | LRTV | LRTDTV | 3DTNN | LRTFDFR | ITSR | NG-meet | FGSLR$_{1/2}$ | Proposed |
|---|---|---|---|---|---|---|---|---|---|
| Urban | 12.6086 | 12.7252 | 13.7804 | 12.8966 | 12.5470 | 13.5549 | 13.0690 | 12.6033 | **12.4799** |
| EO-1 | 14.4493 | 13.9610 | 14.5094 | 12.7535 | 14.8986 | 15.9927 | 13.5869 | 13.7198 | **12.5693** |
| PaviaU | 14.8655 | 16.4829 | 15.3685 | 14.6113 | 14.8808 | 16.4509 | 15.7090 | 15.0798 | **14.5709** |

In conclusion, for these results on the real Urban, EO-1, and PaviaU datasets, the proposed method shows the best visual and quantitative denoising performance.

## V. DISCUSSION

### A. Parameter Analysis

As we know, the results of the prior-based denoising models are usually influenced by the model parameters, and choosing the appropriate parameters also has very important influence to the final denoising results.

Clearly, the proposed model (11) has four important parameters, namely, $\alpha_1$, $\alpha_2$, $\lambda_1$, and $\lambda_2$. In addition, in our experiments, we set the penalty parameters $\mu_1 = \alpha_1 \times 10^{-2}$, $\mu_2 = \alpha_2 \times 10^{-2}$, and $\eta = 0.5$. Moreover, the maximum number of iterations $MaxIter$ is selected empirically as 90. More specifically, the sensitivity of parameters $\alpha_1$, $\alpha_2$, $\lambda_1$, and $\lambda_2$ is discussed for the proposed method as follows.

Thus, Fig. 13 shows the sensitivity analysis of the proposed method by studying the MPSNR and MSSIM results versus parameters $\alpha_1$, $\alpha_2$, $\lambda_1$, and $\lambda_2$ particularly on the simulated PaviaC dataset under Case 6. It can be clearly seen from Fig. 13 that the different setting of parameters $\alpha_1$, $\alpha_2$, $\lambda_1$, and $\lambda_2$ can affect the MPSNR and MSSIM results of the proposed method. Based on this, for the setting of parameters $\alpha_1$, $\alpha_2$, $\lambda_1$, and $\lambda_2$ in our experiments, it is suggested that the values of $\alpha_1$, $\alpha_2$, $\lambda_1$, and $\lambda_2$ should be selected in the intervals of $[0.001, 0.01]$, $[0.001, 0.01]$, $[0.01, 0.1]$ and $[1, 10]$, respectively.

### B. Influence of Proposed SGTNNLR Prior Term (9) With Different Setting of $\alpha_1$ and $\alpha_2$

Moreover, we also discuss the influence of the proposed spatial gradient-based TNN low-rank (SGTNNLR) prior term (9) with different setting of $\alpha_1$ and $\alpha_2$ on the simulated PaviaC dataset under Case 6, which aims to analyze how the spatial horizontal gradient-based tensor low-rank term $\|\nabla_1 \mathcal{X}\|_{\mathrm{TNN}_1}$

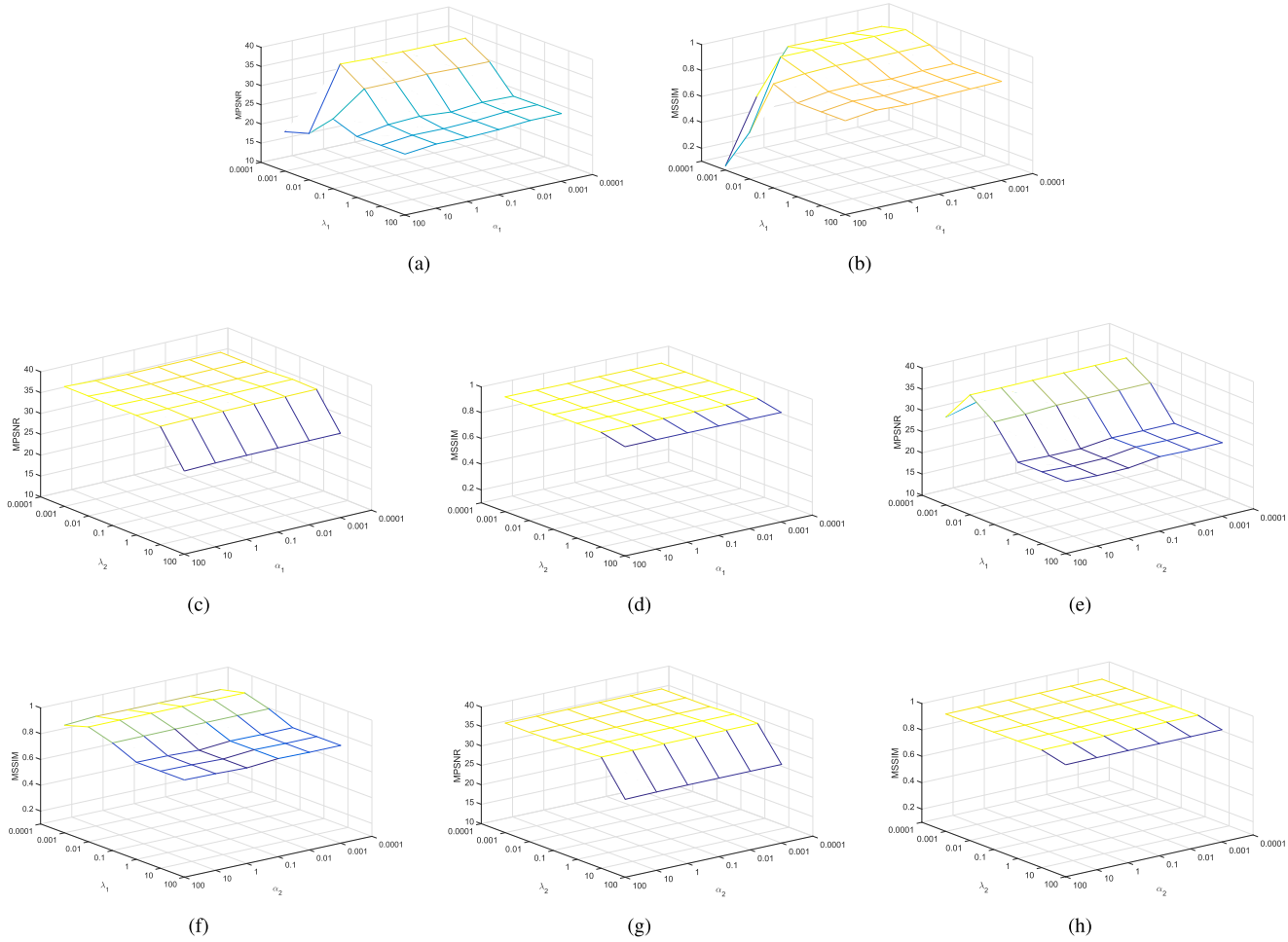


Fig. 13. Sensitivity analysis of parameters $\alpha_1$, $\alpha_2$, $\lambda_1$, and $\lambda_2$ of the proposed method on the simulated PaviaC dataset under Case 6. (a) MPSNR versus $\alpha_1$ and $\lambda_1$. (b) SSIM versus $\alpha_1$ and $\lambda_1$. (c) MPSNR versus $\alpha_1$ and $\lambda_2$. (d) SSIM versus $\alpha_1$ and $\lambda_2$. (e) MPSNR versus $\alpha_2$ and $\lambda_1$. (f) SSIM versus $\alpha_2$ and $\lambda_1$. (g) MPSNR versus $\alpha_2$ and $\lambda_2$. (h) SSIM versus $\alpha_2$ and $\lambda_2$.

TABLE VI
ANALYSIS OF PROPOSED SGTNNLR PRIOR TERM (9) WITH DIFFERENT SETTING OF $\alpha_1$ AND $\alpha_2$ ON THE SIMULATED PAVIAC DATASET UNDER CASE 6

| | MPSNR | MSSIM | SAM |
|---|---|---|---|
| SGTNNLR with $\alpha_1 = 0$ | 37.96 | 0.9596 | 2.9090 |
| SGTNNLR with $\alpha_2 = 0$ | 38.02 | 0.9630 | 2.9073 |
| SGTNNLR with $\alpha_1 \neq 0$ and $\alpha_2 \neq 0$ | **38.68** | **0.9789** | **2.2321** |

TABLE VII
ANALYSIS OF PROPOSED MODEL (11) WITH DIFFERENT SPECTRAL AND SPATIAL GRADIENT TRANSFORMS ON THE SIMULATED PAVIAC DATASET UNDER CASE 6

| | MPSNR | MSSIM | SAM |
|---|---|---|---|
| Model 1 | 29.53 | 0.9176 | 6.0831 |
| Model 2 | 36.12 | 0.9649 | 2.7164 |
| Model 3 | **38.68** | **0.9789** | **2.2321** |

TABLE VIII
ANALYSIS OF INFLUENCE OF THE DFT OF THE PROPOSED SGTNNLR PRIOR TERM (9) ON THE SIMULATED PAVIAC DATASET UNDER CASE 6

| | MPSNR | MSSIM | SAM |
|---|---|---|---|
| SGTNNLR without DFT | 36.78 | 0.9668 | 2.9958 |
| SGTNNLR with DFT | **38.68** | **0.9789** | **2.2321** |

and the spatial vertical gradient-based tensor low-rank term $\|\nabla_2\mathcal{X}\|_{\mathrm{TNN}_2}$ affect the denoising performance separately.

Thus, we consider the following three methods:

i) SGTNNLR with only $\|\nabla_1\mathcal{X}\|_{\mathrm{TNN}_1}$, i.e., SGTNNLR with $\alpha_2 = 0$,

ii) SGTNNLR with only $\|\nabla_2\mathcal{X}\|_{\mathrm{TNN}_2}$, i.e., SGTNNLR with $\alpha_1 = 0$,

iii) SGTNNLR with both $\|\nabla_1\mathcal{X}\|_{\mathrm{TNN}_1}$ and $\|\nabla_2\mathcal{X}\|_{\mathrm{TNN}_2}$, i.e., SGTNNLR with $\alpha_1 \neq 0$ and $\alpha_2 \neq 0$.

As we can see from the results of the above three methods on the simulated PaviaC dataset under Case 6 given in Table VI, the SGTNNLR term with both spatial horizontal and vertical gradients-based tensor low-rank terms (i.e., SGTNNLR with $\alpha_1 \neq 0$ and $\alpha_2 \neq 0$) gives the best results, and the spatial horizontal gradient-based tensor low-rank term (i.e., SGTNNLR with $\alpha_2 = 0$) and the spatial vertical gradient-based tensor low-rank term (i.e., SGTNNLR with $\alpha_1 = 0$) can both affect the denoising performance at different degrees, which both play

TABLE IX
COMPARISONS OF CPU TIME (IN SECONDS) ON DIFFERENT HSI DATASETS

| HSI Datasets | Size | LRMR | LRTV | LRTDTV | 3DTNN | LRTFDFR | ITSR | NG-meet | FGSLR$_{1/2}$ | Proposed |
|---|---|---|---|---|---|---|---|---|---|---|
| PaviaC | $200 \times 200 \times 80$ | 24.84 | 60.82 | 65.07 | 77.34 | 57.24 | 901.92 | 46.09 | 103.87 | 339.45 |
| WDC | $256 \times 256 \times 191$ | 85.06 | 255.17 | 272.84 | 404.08 | 178.70 | 4371.85 | 132.61 | 1600.26 | 1522.01 |
| Urban | $207 \times 207 \times 210$ | 57.98 | 171.79 | 212.96 | 377.80 | 150.58 | 2989.24 | 63.65 | 1271.26 | 853.54 |
| EO-1 | $200 \times 200 \times 166$ | 47.22 | 114.37 | 251.61 | 228.58 | 106.43 | 2671.24 | 70.80 | 191.33 | 537.84 |
| PaviaU | $610 \times 340 \times 103$ | 149.17 | 869.75 | 502.70 | 304.86 | 548.88 | 7232.92 | 467.40 | 384.06 | 2246.22 |

important roles in the proposed SGTNNLR prior term (9) for HSI restoration.

### C. Influence of the Spectral and Spatial Gradient Transforms of the Proposed Model

Clearly, the low-rank modeling of proposed model is investigated in the spectral and spatial gradient domains. Thus, we further discuss the influence of spectral and spatial gradient transforms of the proposed model (11) on the simulated PaviaC dataset under Case 6.

Thus, we consider the following three models:

*Model 1*: Proposed model (11) without the spectral gradient transform, i.e., Term (5) without the spectral gradient transform as $\lambda_2\|\text{unfold}_3(\mathcal{X})\|_{\mathbf{w},*}$.

*Model 2*: Proposed model (11) without the spatial gradient transform, i.e., Term (9) without the spatial gradient transform as $\sum_{k=1}^{2}\alpha_k\|\mathcal{X}\|_{\text{TNN}_k}$.

*Model 3*: Proposed model (11) with both the spectral and spatial gradient transforms in Term (5) and Term (9).

As clearly given in Table VII, Model 3, i.e., the proposed model (11) with both the spectral and spatial gradient transforms, gives the best results, and the spectral and spatial gradient transforms can both affect the performance at different degrees, which shows than the spectral and spatial gradient transforms both play important roles in the proposed model (11) for the HSI restoration.

### D. Influence of the DFT of Proposed SGTNNLR Prior Term (9)

Moreover, we discuss the influence of DFT of the proposed SGTNNLR prior term (9) on the simulated PaviaC dataset under Case 6, where the following two methods are considered: i) SGTNNLR without DFT, and ii) SGTNNLR with DFT.

As clearly provided in Table VIII, SGTNNLR with DFT give better results than those of SGTNNLR without DFT, which thus shows that the DFT also plays an important role in the proposed SGTNNLR prior term (9) for HSI restoration.

### E. Convergence Analysis

Moreover, the convergence of the proposed method is also analyzed. To this end, the MPSNR and MSSIM results versus iterations on the simulated PaviaC and WDC datasets under Case 6 are representatively provided in Fig. 14 for the convergence analysis.

As obviously shown in Fig. 14, the values of MPSNR and MSSIM first increase with the increase of iterations, and then reach a relatively stable state, which is convergent finally. Therefore, the convergence of the proposed method can be further validated.

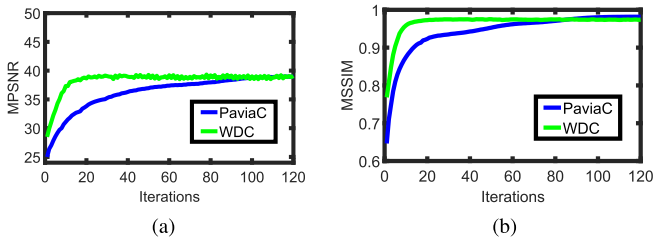


Fig. 14. Convergence curves of MPSNR and MSSIM versus iterations of the proposed method on the simulated PaviaC and WDC datasets under Case 6. (a) MPSNR versus iterations. (b) MSSIM versus iterations.

### F. Analysis of Computational Complexity

Furthermore, the computational complexity of our proposed Algorithm 1 is also analyzed, which can be separately analyzed by the following five subproblems:

1) For the solution of $\mathcal{S}^{(i+1)}$ subproblem via (15), it has the complexity of $O(n_1n_2n_3)$ for each iteration.

2) For the solution of $\mathcal{L}^{(i+1)}$ via (18) and (20), it has the complexity of $O(n_1n_2n_3^2)$ for each iteration.

3) For the solution of $\mathcal{W}_1^{(i+1)}$ and $\mathcal{W}_2^{(i+1)}$ via (22), they both have the complexity of $O(n_1n_2n_3(\log(n_1n_2n_3)+\min(n_1,n_2)+\min(n_2,n_3)+\min(n_3,n_1)))$ for each iteration.

4) For the solution of $\mathcal{X}^{(i+1)}$ via (24), it has the complexity of $O(n_1n_2n_3\log(n_1n_2n_3))$ for each iteration.

5) For the updating of $\mathcal{H}_1^{(i+1)}$, $\mathcal{H}_2^{(i+1)}$, and $\mathcal{U}^{(i+1)}$ via (25), they all have the complexity of $O(n_1n_2n_3)$ for each iteration.

Thus, the total computational complexity of our Algorithm 1 is $O(MaxIter(n_1n_2n_3(\log(n_1n_2n_3)+\min(n_1,n_2)+\min(n_2,n_3)+\min(n_3,n_1))+n_1n_2n_3^2+n_1n_2n_3\log(n_1n_2n_3)+n_1n_2n_3))$, where $MaxIter$ denotes the number of iterations.

### G. Comparisons of CPU Time

Finally, the detailed comparisons of CPU time of different approaches on different HSI datasets are given in Table IX. As given in Table IX, LRMR always spends the shortest CPU time, whereas ISTR always spends the longest CPU time. Clearly, since the proposed model is much more complex than LRMR, then the proposed method spends much more CPU time than LRMR, but much less than ISTR, which shows some competitiveness with the other approaches.

## VI. Conclusion

In this article, we have proposed a novel and effective tensor-based HSI restoration model with low-rank modeling in gradient domains by using the tensor modeling theory. Clearly, we propose the spectral gradient-based weighted nuclear norm low-rank prior term for the spectral low-rank modeling of HSI in spectral gradient domain. More specifically, we particularly propose the spatial gradient-based TNN low-rank prior term for the spatial low-rank modeling of HSI in spatial gradient domain. Moreover, the proposed model is effectively optimized by the ADMM method. Finally, a lot of denoising results on both simulated and real HSI datasets clearly demonstrate that the proposed method is superior to many state-of-the-art denoising methods in the aspects of visual and quantitative comparisons. More importantly, the proposed method is much more effective and robust for the removal of the stripes and deadlines.

## References


[1] B. Rasti et al., "Feature extraction for hyperspectral imagery: The evolution from shallow to deep: Overview and toolbox," *IEEE Geosci. Remote Sens. Mag.*, vol. 8, no. 4, pp. 60–88, Dec. 2020.

[2] X. Zhang, S. Chen, P. Zhu, X. Tang, J. Feng, and L. Jiao, "Spatial pooling graph convolutional network for hyperspectral image classification," *IEEE Trans. Geosci. Remote Sens.*, vol. 60, 2022, Art. no. 5521315.

[3] M. Zhao, S. Shi, J. Chen, and N. Dobigeon, "A 3-D-CNN framework for hyperspectral unmixing with spectral variability," *IEEE Trans. Geosci. Remote Sens.*, vol. 60, 2022, Art. no. 5521914.

[4] S. Yang and Z. Shi, "Hyperspectral image target detection improvement based on total variation," *IEEE Trans. Geosci. Remote Sens.*, vol. 25, no. 5, pp. 2249–2258, May 2016.

[5] J. Liu, Z. Wu, L. Xiao, and X. Wu, "Model inspired autoencoder for unsupervised hyperspectral image super-resolution," *IEEE Trans. Geosci. Remote Sens.*, vol. 60, pp. 1–12, 2022.

[6] D. Shen, J. Liu, Z. Wu, J. Yang, and L. Xiao, "ADMM-HFNet: A matrix decomposition-based deep approach for hyperspectral image fusion," *IEEE Trans. Geosci. Remote Sens.*, vol. 60, pp. 1–17, 2022.

[7] X.-T. Li, X.-L. Zhao, T.-X. Jiang, Y.-B. Zheng, T.-Y. Ji, and T.-Z. Huang, "Low-rank tensor completion via combined non-local self-similarity and low-rank regularization," *Neurocomputing*, vol. 367, pp. 1–12, 2019.

[8] H. Zhang, L. Liu, W. He, and L. Zhang, "Hyperspectral image denoising with total variation regularization and nonlocal low-rank tensor decomposition," *IEEE Trans. Geosci. Remote Sens.*, vol. 58, no. 5, pp. 3071–3084, May 2020.

[9] T. Hu, W. Li, N. Liu, R. Tao, F. Zhang, and P. Scheunders, "Hyperspectral image restoration using adaptive anisotropy total variation and nuclear norms," *IEEE Trans. Geosci. Remote Sens.*, vol. 59, no. 2, pp. 1516–1533, Feb. 2021.

[10] K. Dabov, A. Foi, V. Katkovnik, and K. Egiazarian, "Image denoising by sparse 3-D transform-domain collaborative filtering," *IEEE Trans. Image Process.*, vol. 16, no. 8, pp. 2080–2095, Aug. 2007.

[11] M. Elad and M. Aharon, "Image denoising via sparse and redundant representations over learned dictionaries," *IEEE Trans. Image Process.*, vol. 15, no. 12, pp. 3736–3745, Dec. 2006.

[12] A. Buades, B. Coll, and J.-M. Morel, "A non-local algorithm for image denoising," in *Proc. IEEE Conf. Comput. Vis. Pattern Recognit.*, 2005, pp. 60–65.

[13] B. K. Shreyamsha Kumar, "Image denoising based on non-local means filter and its method noise thresholding," *Signal, Image Video Process.*, vol. 7, no. 6, pp. 1211–1227, 2013.

[14] A. Danielyan, A. Foi, V. Katkovnik, and K. Egiazarian, "Denoising of multispectral images via nonlocal groupwise spectrum-PCA," in *Proc. Conf. Colour Graph. Imag., Vis.*, 2010, pp. 261–266.

[15] M. Maggioni, V. Katkovnik, K. Egiazarian, and A. Foi, "Nonlocal transform-domain filter for volumetric data denoising and reconstruction," *IEEE Trans. Image Process.*, vol. 22, no. 1, pp. 119–133, Jan. 2013.

[16] Y. Qian and M. Ye, "Hyperspectral imagery restoration using nonlocal spectral-spatial structured sparse representation with noise estimation," *IEEE J. Sel. Topics Appl. Earth Observ. Remote Sens.*, vol. 6, no. 2, pp. 499–515, Apr. 2013.

[17] Y. Peng, D. Meng, Z. Xu, C. Gao, Y. Yang, and B. Zhang, "Decomposable nonlocal tensor dictionary learning for multispectral image denoising," in *Proc. IEEE Conf. Comput. Vis. Pattern Recognit.*, 2014, pp. 2949–2956.

[18] E.-J. Candes, X. Li, Y. Ma, and J. Wright, "Robust principal component analysis?," *J. ACM*, vol. 58, no. 3, pp. 1–37, 2011.

[19] H. Zhang, W. He, L. Zhang, H. Shen, and Q. Yuan, "Hyperspectral image restoration using low-rank matrix recovery," *IEEE Trans. Geosci. Remote Sens.*, vol. 52, no. 8, pp. 4729–4743, Aug. 2014.

[20] Y. Chen, Y. Guo, Y. Wang, D. Wang, C. Peng, and G. He, "Denoising of hyperspectral images using nonconvex low rank matrix approximation," *IEEE Trans. Geosci. Remote Sens.*, vol. 55, no. 9, pp. 5366–5380, Sep. 2017.

[21] R. Zhu, M. Dong, and J.-H. Xue, "Spectral nonlocal restoration of hyperspectral images with low-rank property," *IEEE J. Sel. Topics Appl. Earth Observ. Remote Sens.*, vol. 8, no. 6, pp. 3062–3067, Jun. 2015.

[22] W. He, H. Zhang, L. Zhang, and H. Shen, "Hyperspectral image denoising via noise-adjusted iterative low-rank matrix approximation," *IEEE J. Sel. Topics Appl. Earth Observ. Remote Sens.*, vol. 8, no. 6, pp. 3050–3061, Jun. 2015.

[23] M. Wang, J. Yu, J.-H. Xue, and W. Sun, "Denoising of hyperspectral images using group low-rank representation," *IEEE J. Sel. Topics Appl. Earth Observ. Remote Sens.*, vol. 9, no. 9, pp. 4420–4427, Sep. 2016.

[24] F. Fan, Y. Ma, C. Li, X. Mei, J. Huang, and J. Ma, "Hyperspectral image denoising with superpixel segmentation and low-rank representation," *Inf. Sci.*, vol. 397, pp. 48–68, 2017.

[25] L.-I. Rudin, S. Osher, and E. Fatemi, "Nonlinear total variation based noise removal algorithms," *Phys. D, Nonlinear Phenomena*, vol. 60, pp. 259–268, 1992.

[26] H. Zhang, "Hyperspectral image denoising with cubic total variation model," *ISPRS Ann. Photogramm. Remote Sens. Spat. Inf. Sci.*, vol. 7, pp. 95–98, 2012.

[27] Q. Yuan, L. Zhang, and H. Shen, "Hyperspectral image denoising employing a spectral-spatial adaptive total variation model," *IEEE Trans. Geosci. Remote Sens.*, vol. 50, no. 10, pp. 3660–3677, Oct. 2012.

[28] J. Li, Q. Yuan, H. Shen, and L. Zhang, "Hyperspectral image recovery employing a multidimensional nonlocal total variation model," *Signal Process.*, vol. 111, pp. 230–248, 2015.

[29] H. K. Aggarwal and A. Majumdar, "Hyperspectral image denoising using spatio-spectral total variation," *IEEE Geosci. Remote Sens. Lett.*, vol. 13, no. 3, pp. 442–446, Mar. 2016.

[30] W. He, H. Zhang, L. Zhang, and H. Shen, "Total-variation-regularized low-rank matrix factorization for hyperspectral image restoration," *IEEE Trans. Geosci. Remote Sens.*, vol. 54, no. 1, pp. 178–188, Jan. 2016.

[31] Q. Wang, Z. Wu, J. Jin, T. Wang, and Y. Shen, "Low rank constraint and spatial spectral total variation for hyperspectral image mixed denoising," *Signal Process.*, vol. 142, pp. 11–26, 2018.

[32] W. He, H. Zhang, H. Shen, and L. Zhang, "Hyperspectral image denoising using local low-rank matrix recovery and global spatial-spectral total variation," *IEEE J. Sel. Topics Appl. Earth Observ. Remote Sens.*, vol. 11, no. 3, pp. 713–729, Mar. 2018.

[33] N. Renard, S. Bourennane, and J. Blanc-Talon, "Denoising and dimensionality reduction using multilinear tools for hyperspectral images," *IEEE Geosci. Remote Sens. Lett.*, vol. 5, no. 2, pp. 138–142, Apr. 2008.

[34] Y. Wang, J. Peng, Q. Zhao, Y. Leung, X.-L. Zhao, and D. Meng, "Hyperspectral image restoration via total variation regularized low-rank tensor decomposition," *IEEE J. Sel. Topics Appl. Earth Observ. Remote Sens.*, vol. 11, no. 4, pp. 1227–1243, Apr. 2018.

[35] Y.-B. Zheng, T.-Z. Huang, X.-L. Zhao, Y. Chen, and W. He, "Double-factor-regularized low-rank tensor factorization for mixed noise removal in hyperspectral image," *IEEE Trans. Geosci. Remote Sens.*, vol. 58, no. 12, pp. 8450–8464, Dec. 2020.

[36] X. Gong, W. Chen, and J. Chen, "A low-rank tensor dictionary learning method for hyperspectral image denoising," *IEEE Trans. Signal Process.*, vol. 68, pp. 1168–1180, 2020.

[37] Y. Chang, L. Yan, X.-L. Zhao, H. Fang, Z. Zhang, and S. Zhong, "Weighted low-rank tensor recovery for hyperspectral image restoration," *IEEE Trans. Cybern.*, vol. 50, no. 11, pp. 4558–4572, Nov. 2020.

[38] H. Zeng, X. Xie, and J. Ning, "Hyperspectral image denoising via global spatial-spectral total variation regularized nonconvex local low-rank tensor approximation," *Signal Process.*, vol. 178, pp. 1–16, 2021.

[39] L.-R. Tucker, "Some mathematical notes on three-mode factor analysis," *Psychometrika*, vol. 31, pp. 279–311, 1966.
[40] R.-A. Harshman, "Foundations of the PARAFAC procedure: Models and conditions for an "explanatory" multimodal factor analysis," Univ. California at Los Angeles: Westwood, 1970, pp. 1–84.
[41] X. Guo, X. Huang, L. Zhang, and L. Zhang, "Hyperspectral image noise reduction based on rank-1 tensor decomposition," *ISPRS J. Photogramm. Remote Sens.*, vol. 83, no. 9, pp. 50–63, 2013.
[42] J. Xue and Y. Zhao, "Rank-1 tensor decomposition for hyperspectral image denoising with nonlocal low-rank regularization," in *Proc. Int. Conf. Mach. Vis. Inf. Technol.*, 2017, pp. 40–45.
[43] X. Bai, F. Xu, L. Zhou, Y. Xing, L. Bai, and J. Zhou, "Nonlocal similarity based nonnegative tucker decomposition for hyperspectral image denoising," *IEEE J. Sel. Top. Appl. Earth Observ. Remote Sens.*, vol. 11, no. 3, pp. 701–712, Mar. 2018.
[44] X. Liu, S. Bourennane, and C. Fossati, "Denoising of hyperspectral images using the PARAFAC model and statistical performance analysis," *IEEE Trans. Geosci. Remote Sens.*, vol. 50, no. 10, pp. 3717–3724, Oct. 2012.
[45] J. Xue, Y. Zhao, W. Liao, and J.-C. Chan, "Nonlocal low-rank regularized tensor decomposition for hyperspectral image denoising," *IEEE Trans. Geosci. Remote Sens.*, vol. 57, no. 7, pp. 5174–5189, Jul. 2019.
[46] Y. Chen, W. He, N. Yokoya, T. Huang, and X. Zhao, "Nonlocal tensor-ring decomposition for hyperspectral image denoising," *IEEE Trans. Geosci. Remote Sens.*, vol. 58, no. 2, pp. 1348–1362, Feb. 2020.
[47] M.-E. Kilmer and C.-D. Martin, "Factorization strategies for third-order tensors," *Linear Algebra Appl.*, vol. 435, no. 3, pp. 641–658, 2011.
[48] Z. Zhang, G. Ely, S. Aeron, N. Hao, and M. Kilmer, "Novel methods for multilinear data completion and de-noising based on tensor-SVD," in *Proc. IEEE Conf. Comput. Vis. Pattern Recognit.*, 2014, pp. 3842–3849.
[49] Y. Zheng, T. Huang, X. Zhao, T. Jiang, T. Ma, and T. Ji, "Mixed noise removal in hyperspectral image via low-fibered-rank regularization," *IEEE Trans. Geosci. Remote Sens.*, vol. 58, no. 1, pp. 734–749, Jan. 2020.
[50] W. Kong, Y. Song, and J. Liu, "Hyperspectral image denoising via framelet transformation based three-modal tensor nuclear norm," *Remote. Sens.*, vol. 13, no. 19, 2021, Art. no. 3829.
[51] Y. Chen, T. Huang, W. He, X. Zhao, H. Zhang, and J. Zeng, "Hyperspectral image denoising using factor group sparsity-regularized nonconvex low-rank approximation," *IEEE Trans. Geosci. Remote Sens.*, vol. 60, 2022, Art. no. 5515916.
[52] J. Xue et al., "Multilayer sparsity-based tensor decomposition for low-rank tensor completion," *IEEE Trans. Neural Netw. Learn. Syst.*, vol. 33, no. 11, pp. 6916–6930, Nov. 2022.
[53] J. Xue, Y. Zhao, Y. Bu, J. C.-W. Chan, and S. G. Kong, "When Laplacian scale mixture meets three-layer transform: A parametric tensor sparsity for tensor completion," *IEEE Trans. Cybern.*, vol. 52, no. 12, pp. 13887–13901, Dec. 2022, doi: 10.1109/TCYB.2021.3140148.
[54] H. Zeng, J. Xue, H. Luong, and W. Philips, "Multimodal core tensor factorization and its applications to low-rank tensor completion," *IEEE Trans. Multimedia*, early access, 2022, doi: 10.1109/TMM.2022.3216746.
[55] Y. Chang, L. Yan, H. Fang, S. Zhong, and W. Liao, "HSI-DeNet: Hyperspectral image restoration via convolutional neural network," *IEEE Trans. Geosci. Remote Sens.*, vol. 57, no. 2, pp. 667–682, Feb. 2019.
[56] Q. Yuan, Q. Zhang, J. Li, H. Shen, and L. Zhang, "Hyperspectral image denoising employing a spatial-spectral deep residual convolutional neural network," *IEEE Trans. Geosci. Remote Sens.*, vol. 57, no. 2, pp. 1205–1218, Feb. 2019.
[57] J. Peng, Q. Xie, Q. Zhao, Y. Wang, L. Yee, and D. Meng, "Enhanced 3DTV regularization and its applications on HSI denoising and compressed sensing," *IEEE Trans. Image Process.*, vol. 29, pp. 7889–7903, 2020.
[58] H. Lu, Q. Liu, M. Zhang, Y. Wang, and X. Deng, "Gradient-based low rank method and its application in image inpainting," *Multimed. Tools. Appl.*, vol. 77, no. 5, pp. 5969–5993, 2018.
[59] S. Gu, Q. Xie, D. Meng, W. Zuo, X. Feng, and L. Zhang, "Weighted nuclear norm minimization and its applications to low level vision," *Int. J. Comput. Vis.*, vol. 121, no. 2, pp. 183–208, 2017.
[60] Q. Xie et al., "Multispectral images denoising by intrinsic tensor sparsity regularization," in *Proc. IEEE Conf. Comput. Vis. Pattern Recognit.*, 2016, pp. 1692–1700.
[61] W. He, Q. Yao, C. Li, N. Yokoya, and Q. Zhao, "Non-local meets global: An integrated paradigm for hyperspectral denoising," in *Proc. IEEE Conf. Comput. Vis. Pattern Recognit.*, 2019, pp. 6861–6870.
[62] J. Yang, Y. Zhao, C. Yi, and J. C.-W. Chan, "No-reference hyperspectral image quality assessment via quality-sensitive features learning," *Remote Sens.*, vol. 9, no. 4, pp. 1–24, 2017.

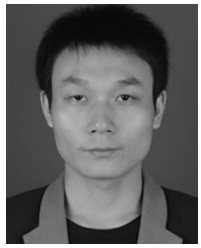

**Pengfei Liu** received the B.S. degree in applied mathematics from Hefei Normal University, Hefei, China, in 2011, and the Ph.D. degree in computer science and technology from Nanjing University of Science and Technology, Nanjing, China, in 2016.

He is currently an Associate Professor with the School of Computer Science, Nanjing University of Posts and Telecommunications, Nanjing, China. His research interests include image processing and remote sensing.

**Lanlan Liu** received the B.S. degree in information and computing sciences from Hubei University, Wuhan, China, in 2020. She is currently working toward the M.S. degree in computer science and technology with the School of Computer Science, Nanjing University of Posts and Telecommunications, Nanjing, China.

Her research interests include remote sensing and hyperspectral image restoration.

**Liang Xiao** (Member, IEEE) received the B.S. degree in applied mathematics and the Ph.D. degree in computer science from Nanjing University of Science and Technology (NJUST), Nanjing, China, in 1999 and 2004, respectively.

He is currently a Professor with the School of Computer Science and Engineering, NJUST. His research interests include image processing, computer vision, machine learning, and remote sensing.